



Available online at www.sciencedirect.com

ScienceDirect

Geochimica et Cosmochimica Acta 297 (2021) 158-178

Geochimica et Cosmochimica Acta

www.elsevier.com/locate/gca

A first look at Ge/Si partitioning during amorphous silica precipitation: Implications for Ge/Si as a tracer of fluid-silicate interactions

Nicole M. Fernandez a,b,*, Alida Perez-Fodich c, Louis A. Derry b,d, Jennifer L. Druhan a

a Department of Geology, University of Illinois at Urbana Champaign, Urbana, IL 61801, USA
 b Université de Paris, Institut de Physique du Globe de Paris, CNRS, F-75005 Paris, France
 c Department of Geology, University of Chile, Santiago, Chile
 d Department of Earth and Atmospheric Sciences, Cornell University, Ithaca, NY 14853, USA

Received 5 August 2020; accepted in revised form 6 January 2021; Available online 16 January 2021

Abstract

We measured germanium-silicon (Ge/Si) ratios in both fluid and solid phases using a series of highly constrained amorphous silica precipitation experiments at 20 °C and neutral pH for a wide range of seed crystal surface areas. Silicon isotope data ($\delta^{30/28}$ Si) for these experiments were previously reported by Fernandez et al. (2019). A distinct lag in the onset of Ge/Si partitioning relative to δ^{30} Si fractionation during active amorphous silica growth indicated that Ge incorporation rates were orders of magnitude slower than silicon precipitation rates. Slow Ge kinetics give the appearance of conservative behavior over short experimental timescales (\sim 30 days). A major outcome from these observations was the existence of distinct equilibration timescales between Ge/Si and δ^{30} Si. Further, these experimental results provide the first documented evidence of rate dependent behavior in Ge partition coefficients. Successful application of a modified solid solution model, initially developed for characterizing stable isotope fractionation, indicates that a common fractionation model theory is able to describe both Ge/Si and δ^{30} Si partitioning. Numerical simulations conducted at longer timescales (1–1000 years) predict eventual Ge incorporation into the mineral surface, but this occurs when the system is in close proximity to equilibrium conditions. These long-term predictions underscore the potential of Ge as a (near)equilibrium tracer in complement to the mixed kinetic and equilibrium signatures recorded by δ^{30} Si. Our findings illustrate the viability of a combined Ge/Si– δ^{30} Si multi-tracer approach for constraining silicate mineral formation across a variety of terrestrial and marine systems.

Keywords: Germanium; Silicon; Ge/Si; Si stable isotopes; Trace element partitioning; Stable isotope fractionation; Amorphous silica precipitation; Batch experiments; Geochemical modeling

1. INTRODUCTION

Shared characteristics between trace element germanium (Ge) and major element silicon (Si) make germanium to

silicon (Ge/Si) ratios valuable tracers of the global silicon cycle (Froelich et al., 1985, 1992; Mortlock and Froelich, 1987; Murnane and Stallard, 1990; Hammond et al., 2000; King et al., 2000; Kurtz et al., 2002; Derry et al., 2005; Baronas et al., 2018). Ge and Si are both group IV elements and have similar electronic configurations as both reside within the "p-block' of the periodic table. They have similar oxygen bond lengths (Si–O and Ge–O are 1.75 and

^{*} Corresponding author at: Department of Earth and Atmospheric Sciences, Cornell University, Ithaca, NY 14853, USA *E-mail address:* n.fernandez@cornell.edu (N.M. Fernandez).

1.64 Å, respectively) and are of similar sizes, where Ge is slightly larger (atomic radius = 0.53 Å) compared to Si (atomic radius = 0.41 Å). These common properties facilitate the incorporation of Ge into secondary silicate phases as a substitute for Si in the same manner commonly observed for other pseudo-isotope trace replacements, such as Sr for Ca in carbonates, following Goldschmidt's principle (Goldschmidt, 1926, 1958). In this respect Ge can be considered as a pseudo-isotope of silicon, imitating Si behavior across the biogeochemical Si cycle from the chemical weathering of rocks to the uptake of diatoms in the oceans and throughout long-term storage as deep marine sediments. Like the silicon stable isotope (δ^{30} Si) tracer, Ge/Si ratios are partitioned due to a distinct subset of biogeochemical processes, notably secondary mineral formation, biological uptake, and adsorption onto Fe-(hydr) oxides. These pathways cause Ge to partition from Si based on compatibility and substitution mechanisms analogous to mass dependent fractionations between heavy 30Si and light ²⁸Si isotopes (Opfergelt et al., 2010; Delvigne et al., 2016; Baronas et al., 2018). The magnitude of partitioning between the reacting phases (i.e., fluid and solids) for Ge/ Si is generally characterized by a partition coefficient $\left(K_D = \frac{Ge/Siproduct}{Ge/Sireactant}\right)$. This is comparable to δ^{30} Si fractionation, described by a fractionation factor ($\alpha = R_{product}$) $R_{reactant}$ where R = $\frac{^{30}\text{Si}}{^{28}\text{Si}}$).

In natural environments, congruent mineral dissolution is not associated with any systematic δ^{30} Si or Ge/Si fractionation (Wada and Wada, 1982; Kurtz et al., 2002). Abiotic silicate mineral precipitation is a major fractionating pathway for both δ^{30} Si (Ziegler et al., 2005a,b; Georg et al., 2006, 2007, 2009; Opfergelt et al., 2012; Pogge von Strandmann et al., 2012; Hughes et al., 2013; Riotte et al., 2018; and others) and Ge/Si (Kurtz et al., 2002; Scribner et al., 2006; Lugolobi et al., 2010; Aguirre et al., 2017; Ameijeiras-Marino et al., 2018; Qi et al., 2019; Perez-Fodich and Derry, 2020). This process distinguishes the compositions of the forming solid phase and surrounding fluid as a function of the rate and extent of mineral growth.

Ge/Si and δ^{30} Si have been shown to co-evolve under terrestrial weathering conditions (Lugolobi et al., 2010; Opfergelt et al., 2010; Delvigne et al., 2016; Baronas et al., 2018, 2020) and, for the most part, the manner in which they fractionate is thought to be comparable. For secondary clays, δ³⁰Si and Ge/Si signatures are typically inversely correlated in that the light ²⁸Si is preferentially incorporated into the newly-formed clay due to kinetic isotope effects and Ge is similarly preferentially partitioned into the solid phase as a result of compatibility with secondary clays at equilibrium ($K_d \sim 10.7$ on average for secondary clays; Kurtz et al., 2002). The result is a secondary clay low in δ^{30} Si, ranging from -2.95 to -0.16% (Ziegler at al., 2005a,b; Georg et al., 2006; Cornelis et al., 2010; Opfergelt et al., 2012; Hughes et al., 2013. Frings et al., 2016; Riotte et al., 2018; and others) and elevated in Ge/ Si, reaching values greater than 5 μmol mol⁻¹ (Kurtz et al., 2002; Lugolobi et al., 2010; Opfergelt et al., 2010; Aguirre et al., 2017; Ameijeiras-Marino et al., 2018; Qi

et al., 2019). Thus, the fluid from which these mineral phases form must become isotopically heavier (i.e., higher δ^{30} Si values) and lower in Ge/Si with respect to the bedrock or minerals which were originally solubilized.

Some circumstances cause distinct δ^{30} Si and Ge/Si behavior. Notably, δ^{30} Si and Ge/Si are decoupled from one another during uptake by vascular plants, where light 28 Si is preferentially incorporated into the phytoliths while Ge is generally excluded. This results in high soil water Ge/Si and δ^{30} Si and correspondingly lower values in phytoliths (Derry et al., 2005; Blecker et al., 2007; Meek et al., 2016). Despite these noted exceptions, we generally anticipate that the underlying fractionation mechanisms for δ^{30} Si and Ge/Si are inherently analogous during mineral neoformation (similar to that proposed for Ca stable isotopes and Sr/Ca ratios; DePaolo, 2011). However, despite numerous examples of δ^{30} Si and Ge/Si co-evolution in the field, the behavior of these two tracers during secondary silicate precipitation has yet to be directly demonstrated.

To explore the extent to which δ^{30} Si and Ge/Si fractionation are influenced by both kinetic and equilibrium effects, including the potential for co-evolution of the mineral surface and fluid in the transition from kinetically controlled to near-equilibrium conditions, we analyzed samples from a series of highly constrained amorphous silica precipitation experiments recently reported by Fernandez et al. (2019). This approach leveraged the relatively rapid kinetics of amorphous silica formation (Geilert et al., 2014; Roerdink et al., 2015) to document δ^{30} Si fractionation behavior under variable or "free-drifting" conditions (i.e., where saturation states and solute compositions are allowed to change with reaction progress) across a range of seed crystal specific surface areas (e.g., a range of growth rates) and solid to fluid ratios. The study showed clear evidence for kinetic isotope fractionation followed by rapid isotopic re-equilibration as a function of the overall precipitation rate and, thus, by extension the surface area of seeds used in the experiments. In this context, the mechanisms of δ³⁰Si fractionation during amorphous silica precipitation were comparable to that of δ^{44} Ca during carbonate formation (Tang et al., 2008; DePaolo 2011). But, due to the free drift nature of the experiments, these data were shown to depend on both chemical (saturation state, solute compositions) and physical (surface area, solid to fluid ratio) characteristics of the system. Thus, the utility of the silicon isotopic tracer incorporates a variety of physiochemical effects and parsing this signature in natural settings could pose a poorly constrained problem if and when all factors are varying.

Viewed in this way, the analogous behavior of Ge/Si ratios offer a promising tool to complement δ^{30} Si if the factors affecting this signature can be similarly constrained within a unified model framework. To test whether δ^{30} Si and Ge/Si follow analogous fractionation pathways for amorphous silica formation, we applied a numerical multi-component geochemical model adapted from the principles of the SRKM (surface reaction kinetic model) proposed by DePaolo (2011) to our "free-drift" experimental data. This model framework has been successfully used in the past to describe δ^{44} Ca and Sr/Ca fractionation in

calcite precipitation experiments (Tang et al., 2008; AlKhatib and Eisenhauer, 2017) and has been recently applied to describe δ^{30} Si fractionation during amorphous silica formation (Roerdink et al., 2015; Fernandez et al., 2019).

This study reports the first direct documentation of the extent of Ge incorporation and Ge/Si fractionation during active amorphous silica precipitation under highly constrained laboratory conditions. This experiment is the first, to our knowledge, to directly parse the effects of kinetically limited mineral growth on Ge/Si relative to δ^{30} Si signatures. Our findings have direct implications for interpretation of Ge/Si ratios observed in a variety of field settings where amorphous silica precipitation exerts a large control on silicon (bio)geochemical cycling. Examples include silicate weathering in the critical zone, hydro(geo)thermal activity, and marine diagenesis and recrystallization.

2. METHODS

2.1. Batch experiments

The samples analyzed in this study were generated from amorphous silica precipitation batch experiments reported in Fernandez et al. (2019). We refer the reader to this prior publication for complete descriptions of the experimental design and initial conditions. To summarize, amorphous silica precipitation experiments were conducted in three closed batch reactors each with a different set of $SiO_{2(s)}$ seed crystal surface areas and solid to fluid silicon mass ratios (50 to 31 $SiO_{2(s)}[g]:SiO_{2(aq)}[g]$) at an ambient temperature of 20 °C. All experiments started at a comparable dissolved SiO_{2(ag)} concentration (5.3 mM) and pH (7.3) and were run for approximately 30 days, resulting in an initial oversaturation of 0.48 ± 0.06 (log Q/K) with respect to SiO_{2(s)}. Each batch reactor contained one of three seed crystal grain sizes, with specific surface areas that will from now on be referred to as high (SSA = $50 \text{ m}^2 \text{ g}^{-1}$), medium (SSA = 0.127 m^2 g^{-1}), and low (SSA = 0.072 m² g^{-1}) experiments. Initial seed Ge/Si ratios for the high, medium, and low surface $0.28 \pm 0.01 \; \mu mol \; mol^{-1}$, were area grains $\pm 0.02 \, \mu \text{mol mol}^{-1}$, and $0.64 \pm 0.02 \, \mu \text{mol mol}^{-1}$, respectively. Starting oversaturated solutions were prepared by dissolving 10 g of high surface area fumed silica grains in 1L of MQ-e water at 90 °C for \sim 1 week until starting SiO_{2(aq)} concentration were reached. Ge was introduced through leaching via the dissolution of these high surface area seeds (Ge/Si = $0.28 \pm 0.01 \,\mu\text{mol mol}^{-1}$) at $90 \,^{\circ}\text{C}$, resulting in a starting Ge:Si content in the fluid of 0.044 $\pm 0.002 \,\mu\text{M}$: $0.00530 \pm 0.00003 \,\text{M}$ (initial fluid Ge/Si ratio $= \sim 8.45 \pm 0.3 \,\mu\text{mol mol}^{-1}$). The difference in seed crystal and starting solution Ge/Si ratios is discussed further in Section 4.1.

The next steps in the preparation of the starting solution followed different protocols depending on the type of surface area seeds used in each batch. For the batch involving high surface area seeds, the starting solution after the predissolution step at 90 °C was cooled directly to 20 °C. In the medium and low surface area batches, the starting solutions were subjected to vacuum filtration to remove the

undissolved high surface area grains and subsequently cooled to 20 °C. In all batches, initially acidic solutions $(pH \sim 4.5)$ were then titrated with 10 mM NaOH to the target starting pH (7.3). This increase in pH to near-neutral values was sufficient to initiate precipitation in the high surface area case. For the low and medium surface area cases, amorphous silica seed crystals of appropriate size were also added in order to start the reaction. In all batches, precipitation occurred onto pre-existing grains homogeneously distributed in solution with starting masses of approximately 4 g for the medium and low surface area batches and 0.5 g for the high surface area batch. Experiments were run for a duration of ~ 30 days while being continuously agitated on a shaker plate. Samples were withdrawn at regular time intervals in aliquots of 2.5 mL using a disposable syringe and 0.22 µm nylon filter. A fraction of the sample (2 mL) was subsequently diluted to 10 mL with ultrapure water in preparation for silicon stable isotope and Ge concentration analyses. Experiments were terminated after the last sample was taken and amorphous silica grains were separated out of the remaining solution via vacuum filtration. Initial experimental conditions across all seed crystal surface areas are reported in Table 1.

2.2. Germanium analyses

Germanium concentrations were analyzed using hydride-generation ICP mass-spectrometry (HG-ICP-MS) (Mortlock and Froelich, 1996; Aguirre et al., 2017) at Cornell University with a custom HG sample introduction system and a Thermo-Finnigan Element 2 ICP-MS. Aqueous samples were prepared by adding an enriched ⁷⁰Ge spike solution and allowed to equilibrate for at least 48 hours at room temperature. The spike solution was added to target a ⁷⁰Ge/⁷⁴Ge ratio of 10, estimated from the Si concentrations. To measure Ge concentrations, the prepared samples were introduced into the hydride generation system with a 4% NaBH₄ solution to reduce aqueous Ge(OH)₄ to volatile GeH₄, passing through an gas-liquid-separation filter along with Ar as carrier gas into the ICP-MS. Germanium was quantified by isotope dilution using the ⁷⁰Ge/⁷⁴Ge ratio. Mass bias and signal drift were corrected using standard sample bracketing. We measured Ge standards at 5, 20, 50, 100 and 200 ng L^{-1} . To cross-check the isotope dilution calculations, standard response curves were generated at m/z = 74 for each Ge concentration. The ⁷⁰Ge/⁷⁴Ge in the spike is equal to 162, thus the contribution from the spike at m/z = 74 is insignificant. Analytical uncertainty for these measurements is approximately 3% RSD (Kurtz et al., 2002; Derry et al., 2005; Lugolobi et al., 2010; Kurtz et al., 2011). The contribution of the spike addition to the uncertainty of Ge measurements is negligible (Heumann, 1988).

2.3. Model design and assumptions

Ge partitioning during amorphous silica precipitation was simulated using the multi-component reactive transport software, CrunchTope (Steefel et al., 2015). The fractionation model framework within CrunchTope uses a

Table 1 Starting conditions for all three amorphous silica precipitation batch experiments.

Physical parameters	High SA	Med SA	Low SA
SiO _{2(aq)} [mM]*	5.3 ± 0.7	5.3 ± 0.4	5.3 ± 0.5
Ge(OH) ₄ [μM] [‡]	0.043 ± 0.001	0.044 ± 0.001	0.046 ± 0.001
$\Omega [\log Q/K]^{\mathbb{Y}}$	-3.95	-3.95	-3.95
GeOH _{4(aq)} [μg] [‡]	0.157 ± 0.003	0.80 ± 0.02	0.83 ± 0.02
GeO _{2(s)} [µg]	0.166 ± 0.003	2.90 ± 0.06	3.35 ± 0.07
$GeO_{2(s)}$: $GeOH_{4(aq)}$ [µg/µg] [†]	1.06 ± 0.03	3.6 ± 0.1	4.0 ± 0.1
S [m ²]*	25 ± 8	0.54 ± 0.02	0.31 ± 0.02

^{*} Fernandez et al. (2019).

two-endmember solid solution (Druhan et al., 2013) to create a simple, binary mechanical mixture between two substituting elements in a solid phase such as rare and major isotopes of a major element (ex. $^{28}\text{Si}_{1-x}^{30}\text{Si}_{x}\text{O}_{2(am)}$) or trace and major elements (ex. $\text{Si}_{1-x}\text{Ge}_{x}\text{O}_{2(am)}$), where x represents the mole fraction of either the rare isotope or trace element. For the purposes of the current study, an ideal solid solution between amorphous GeO_2 and SiO_2 takes the following form (Eq. (1)):

$$\begin{split} &(1-x)\mathrm{Si}(\mathrm{OH})_{4(\mathrm{aq})}\\ &+x\mathrm{Ge}(\mathrm{OH})_{4(\mathrm{aq})}{\rightleftharpoons}(\mathrm{Si}_{(1-x)}\mathrm{Ge}_x)\mathrm{O}_{2(\mathrm{am})}+2\mathrm{H}_2\mathrm{O} \end{split} \tag{1}$$

where Ge in the form of Ge(OH)_{4(aq)} species in solution is shown substituting for Si in amorphous silica, SiO_{2(am)}, in this solid solution stoichiometry and x represents the mole fraction of GeO_{2(am)}. In an ideal solid solution each element (in the case of isotopes, each individual isotope), can substitute for one another in the same site within the crystal structure with negligible changes to the thermodynamic (i.e., entropy of mixing) or physical (i.e., molar volume) aspects of a growing mineral phase (Gresens, 1981; Anderson and Crerar, 1993). Thus, for an ideal solid solution the sum of the activity coefficients must equal 1. Under this ideal solid solution assumption, the mole fraction, x, can then be treated as a variable, which allows for the traditional net TST (transition state theory) rate laws to be recast such that each endmember component can be treated individually as shown below (Eq. (2)):

$$^{Ge}R_{p}{=}^{Ge}X^{Ge}kA{\left(\frac{Ge(OH)_{4(aq)}}{^{Ge}X^{Ge}K_{eq}}-1\right)^{m}} \eqno(2a)$$

$$^{Si}R_{p} {=}^{Si}X^{Si}kA \bigg(\frac{Si(OH)_{4(aq)}}{^{Si}X^{Si}K_{eq}} - 1 \bigg)^{m} \tag{2b}$$

$$^{i}X = \frac{n_{Si,Ge}}{n_{Si} + n_{Ge}} \tag{2c}$$

where the individual TST rate laws (in units of mol s⁻¹) displayed for Ge ($^{\text{Ge}}\mathbf{R}_{\mathbf{p}}$, Eq. (2a)) and Si ($^{\text{Si}}\mathbf{R}_{\mathbf{p}}$, Eq. (2b)) are coupled by the mole fractions for $\text{GeO}_{2(am)}$ and $\text{SiO}_{2(am)}$, $^{i}\mathbf{X}$ (i=Si, Ge), defined by the number of moles of either Ge or Si ($n_{\text{Ge},\text{Si}}$) over the total moles of amorphous silica present (Eq. (2c)). These rate equations are dependent on

the total surface area of the amorphous silica grains (A, [m²]), the rate constants (ik, [moles m⁻² s⁻¹]), the relative activities of the major $(Si(OH)_{4(aq)})$ and trace element (Ge (OH)_{4(aq)}) in solution and their respective equilibrium constants (¹K_{eq}). The affinity dependence, m, is set to 3.5 in this model, based on a sensitivity analysis of the reaction order term (which can range from 1 to > 5 for amorphous silica precipitation, Iler, 1979; Rimstidt and Barnes, 1980; Fleming, 1986; Tobler et al., 2009) performed in Fernandez et al. (2019) for the same experiments. To our knowledge, there is no direct constraint for the value of macross a solid solution between Si and Ge or any other comparable system. Thus, the same reaction order term is imposed for both Si and Ge rate equations to respect the formalism of the ideal solid solution condition and to maintain consistency with the Fernandez et al. (2019) model. Kinetic and equilibrium partition coefficients for Ge, Dkin and D_{EO} , are defined in this model formulation by the ratio of the precipitation rate constants $\binom{Ge_k}{Sl_k}$ and equilibrium constants $\left(\frac{-GeK_{eq}}{NK_{eq}}\right)$, respectively, and are distinct from the overall or 'effective' partition coefficient K_D $\left(\frac{Ge/Si_{solid}}{Ge/Si_{Go,id}}\right)$ defined in Section 1.

This model follows the same fractionation framework initially developed for stable isotopes (Druhan et al., 2013) and successfully applied to Si stable isotope fractionation for the same amorphous silica growth experiments (Fernandez et al., 2019). Importantly, the application of this model to Ge/Si during amorphous silica growth assumes that the behavior of Ge trace element partitioning is analogous to silicon stable isotopes, as has been indicated previously for other systems such as δ^{44} Ca and Sr/Ca during calcite growth. Here, for the first time, we directly test such commonality for the $\delta^{30}Si$ and Ge/Si system. This numerical modeling approach notably allows both fluid and solid phase trace element ratio (Ge/Si) compositions to evolve through time via coupled net precipitation rates and mole fractions (Eq. (2)) within an ideal solid solution framework. For stable isotopes, the underlying assumptions for the mole fraction are valid because isotopic substitution into the crystal structure of a growing solid phase is one of the closest approximations to a true ideality

[‡] Measured fluid Ge concentrations with an analytical uncertainty of 2% RSD.

[¥] Saturation states for GeO₂ calculated using CrunchTope.

[†] Solid to fluid mass ratio calculated as the initial amount of Ge present in both the amorphous silica seed and fluid phase (GeOH₄). Error calculated based on standard error propagation using 2% RSD analytical uncertainty for Ge concentrations measurements.

(Anderson and Crerar, 1993). However, application of the same model to Ge requires consideration of the appropriateness of this ideal solid solution assumption.

2.3.1. The ideal Ge - Si solid solution

The validity of an ideal Ge-Si solid solution for amorphous silica is essentially unknown due to the lack of available thermodynamic information. Shared chemical properties (valence state and inorganic aqueous speciation) between Ge and Si implies that Ge substitution for Si could be reasonably approximated as ideal during secondary siliformation (Capobianco and Watson, 1981; Capiobianco and Navrotsky, 1982; Martin et al., 1996; Pokrovski and Schott, 1998). This recently led Perez-Fodich and Derry (2020) to assume ideality for Ge-Si mixing behavior during kaolinite formation. For the current study (amorphous SiO₂-GeO₂ solid solution) two observations are particularly relevant in our justification of ideality. First, calorimetric data from the Capobianco and Watson (1981) experimental study of Ge partitioning in sodium feldspars indicate that amorphous glasses tend to conform better to an ideal solid solution than their crystalline counterparts. Second, Evans and Derry (2002) found that an ideal solid solution model adequately described the behavior of Ge and Si during hydrothermal quartz precipitation.

Furthermore, Ge/Si in most natural systems is near 10^{-6} whereas 30 Si/ 28 Si is near 0.031, so while Ge is likely to substitute less readily for 28 Si than 30 Si, its relative abundance is 4 orders of magnitude lower. With a molar ratio of 10^{-5} to 10^{-6} between Ge and Si in silicates, such a system approaches the Henry's Law limit of ideal behavior, even when higher concentrations would lead to non-ideality. Thus, an ideal solid solution is a reasonable assumption for Ge–Si binary mixing during amorphous silica growth.

2.3.2. Trace element model parameterization

In this model approach, Ge is treated in the same manner as a rare isotopologue in a stable isotope system, albeit with some important distinctions. For instance, in the treatment of stable isotopes in this framework, the activities of the individual isotopes (²⁸Si and ³⁰Si) must sum up to overall activity of Si in solution. But for trace elements, the activities of Ge and Si are considered independent. Consequently, the kinetic and thermodynamic parameters of both amorphous SiO₂ and GeO₂ must be acquired individually. Amorphous silica is fortunately well-studied, and an abundance of kinetic and thermodynamic data are available from a multitude of carefully conducted laboratory studies (Rimstidt and Barnes, 1980; Fleming, 1986; Gurnarsson and Arnórsson, 2000, Tobler et al., 2009; Geilert et al., 2014; Roerdink et al.2015; Oelze et al.2015; Stamm et al., 2019; Fernandez et al., 2019). Thus, for SiO₂, the precipitation rate and equilibrium constants at 20 °C are well constrained with values of $10^{-9.67}$ moles m⁻² s⁻¹ (Rimstdt and Barnes, 1980) and $10^{-2.7135}$ (Gunnarsson and Arnórsson, 2000), respectively. This makes parameterization of Eq. (2a) straightforward, as was done in Fernandez et al. (2019) for the silicon isotope model. Parameterizing Eq. (2b), however, is more complicated. Experimentally determined thermodynamic data for germanates are scarce and only exist for a few minerals including argutite $(GeO_{2(hex)})$ (Arnórsson 1984; Pokrovski and Schott, 1998) and some chain and phyllo-silicates (Pokrovski and Schott, 1998; Shtenberg et al., 2017 respectively). We are not currently aware of any kinetic data that exists for the formation of $GeO_{2(am)}$. Lacking this necessary data, we rely on estimates for both kinetic and thermodynamic parameters based on our experimental results and the known K_D value of crystalline SiO_2 and GeO_2 phases, respectively.

For the amorphous germanium oxide (GeO₂) solubility constant, any equilibrium partitioning between Ge/Si across equilibrated fluid and solid phases implies that this value is not precisely equal to its SiO₂ counterpart. Assuming applicability to an amorphous solid, we apply the equilibrium model for an ideal binary mixture between crystalline quartz (SiO₂) and argutite GeO₂, Ge_xSi_{1-x}O₂ given by Evans and Derry (2002), which states that:

$$GeO_{2(am)} + 2H_2O \rightleftharpoons GeOH_{4(ag)}$$
 (3a)

$$SiO_{2(am)} + 2H_2O \rightleftharpoons SiOH_{4(aq)}$$
 (3b)

$$\begin{split} ^{Ge}K_{eq(am)} &= \frac{a_{Ge(OH)_{4(aq)}}}{a_{Si(OH)_{4(aq)}}} \times \frac{^{Ge}X}{^{Ge}X} \times ^{Si}K_{eq(am)} \\ &= \frac{\left(Ge/Si\right)_{fluid}}{\left(Ge/Si\right)_{solid}} \times ^{Si}K_{eq(am)} \end{split} \tag{3c}$$

$$\begin{split} ^{Ge}K_{eq(am)} &\approx \frac{^{Ge}K_{sp,argutite}}{^{Si}K_{sp,quartz}} \times \ ^{Si}K_{eq(am)} \\ &= D_{EQ(qtz-argutite)} \times \ ^{Si}K_{eq(am)} \end{split} \tag{3d}$$

where for Eq. (3a) to Eq. (3c), $a_{Ge(OH)4}$ and $a_{Si(OH)4}$ are the activities of germanic and silicic acid at equilibrium, SiX and GeX are the mole fractions of the SiO2 and GeO2 solid phases, and $^{Si}K_{eq(am)}$ is the solubility constant for amorphous silica ($10^{-2.7135}$ M; Gunnarsson and Anórsson, 2000). Through the combination of Eq. (3a) and Eq. (3b) we can estimate the equilibrium constant for amorphous GeO₂ (Eq. (3c)). The known equilibrium partition coefficient between quartz and argutite ($D_{EQ} = {}^{Ge}K_{eq(argutite)}$ / $^{Si}K_{eq(quartz)}$) is defined by their relative equilibrium constants of $10^{-3.9582}$ M (Rimstidt and Barnes, 1980) and $10^{-5.0645}$ M (Pokrovski et al., 2005) respectively at 25 °C. Assuming a comparable partitioning for the amorphous phases and the known solubility constant for amorphous silica, $^{Si}K_{eq(am)}$, the equilibrium constant for amorphous GeO_2 ($^{Ge}K_{eq(am)}$) is estimated to be $10^{-3.8198}$ M (Eq. (3d)). Thus, D_{EO} for amorphous silica using the equilibrium model is 0.08, which corresponds to an "effective" partition coefficient $\left(K_D = \frac{(Ge/Si)_{solid}}{(Ge/Si)_{fluid}}\right)$ of 12.8 through the expression $K_D \approx \frac{1}{D_{EQ}}$ (Eq. (3c) and (3d)). A K_D of 12.8 indicates that amorphous silica at equilibrium should have a final Ge/Si ratio 12.8× higher than the fluid.

Ge kinetics during amorphous silica formation are estimated via a best-fit approximation and sensitivity test using the experimental data reported in this study (Section 4.2). Ge batch model simulations for amorphous silica precipitation were performed for a range of timescales (35–1000 years), surface areas (0.072–50 m² g⁻¹), and Ge precipitation scenarios using identical starting fluid and solid phase Ge/Si ratios, temperature, and pH.

3. RESULTS

3.1. Time evolution of Ge/Si

Measured fluid and solid phase Ge/Si ratios (denoted as (Ge/Si)_{fluid} and (Ge/Si)_{am.silica}, respectively; Table 2), monitored over the experimental duration from 0 to 30 days (Fig. 1), are presented alongside measured dissolved Si concentrations and their corresponding δ^{30} Si values for the high, medium, and low surface area experiments reported by Fernandez et al. (2019). Dissolved silica concentrations (Fig. 1A) decrease with time for all experiments until a metastable equilibrium is attained with respect to the amorphous silica solubility concentration at 20 °C (Gunnarsson and Anórsson, 2000; Fernandez et al., 2019). Correspondingly, fluid Ge concentrations (Ge(OH)4, Table 2) remained relatively constant with time from a starting concentration of 44788 ± 1750 pM (1SD, n = 3) to a final concentration of $41129 \pm 1989 \text{ pM}$ (1SD, n = 3). Of the three batches, the high surface area showed the largest variability (Ge $(OH)_{4,start} - Ge(OH)_{4,end} = 3921 \pm 1156 \text{ pM}$). Time averaged rates for Ge calculated based on the difference in concentrations over a given time interval (Eq. (5) in Fernandez et al., 2019) are \sim 5 orders of magnitude slower ($R_p^{Ge}=10^{-14.3\pm0.6}$ mol m $^{-2}$ s $^{-1}$, n = 3; Table 2) than Si precipitation rates ($R_p^{Si}=10^{-8.9\pm0.5}$ mol m $^{-2}$ s $^{-1}$, n = 3; Table 2). For all experiments (Ge/Si)_{fluid} ratios increase with time and subsequently stabilize at elevated values after approximately 10 days (Fig. 1B). Low and medium surface area (Ge/Si)_{fluid} values correlate strongly with the corresponding δ^{30} Si_{fluid}, effectively displaying the same evolving behavior with time. In contrast, high surface area (Ge/Si)_{fluid} and δ³⁰Si_{fluid} quickly diverge as $\delta^{30} Si_{fluid}$ begins to isotopically reequilibrate towards lower $\delta^{30} Si_{fluid}$ after roughly 1 day (Fernandez et al., 2019). Over the same period of time (Ge/Si)_{fluid} ratios continue to increase and ultimately stabilize to a final (Ge/Si)_{fluid} of 18.95 μmol mol⁻¹, which is higher than the medium (max (Ge/Si)_{fluid} = $14.40 \; \mu mol \; mol^{-1}$ and (Ge/Si)_{fluid} = low (max $12.04 \text{ } \text{umol mol}^{-1}$) surface area batches, respectively.

Evolution of the bulk amorphous silica Ge/Si ratios $((Ge/Si)_{am.silica},\ Fig.\ 1B)$ were calculated based on the cumulative mass of SiO_2 ($N_{SiO_{2(ppt)}}$ where ppt = precipitate; Fernandez et al., 2019) and GeO₂ (N_{GeO_{2(ppt)}}, Table 2) precipitated out of solution onto the pre-existing seeds in the batch reactor. Mass balance calculations show (Ge/Si)_{am.sil}ica to slightly increase throughout the extent of the reaction compared to the measured initial seed Ge/Si ratios (Table 2). The high surface area batch shows the largest shifts in the growing amorphous silica Ge/Si, from initial value of $0.28 \pm 0.01 \; \mu mol \; mol^{-1}$ to a measured final value of $0.33 \pm 0.02 \,\mu\text{mol mol}^{-1}$, which is slightly greater than the analytical uncertainty. This shift to higher (Ge/Si)am.silica values was found to occur after ~ 1 day, by which time dissolved silica concentrations decreased by ~45% (a majority of the total silica ultimately precipitated out of solution). In comparison, the evolution of (Ge/Si)_{am silica} for the lower surface area batches falls within the uncertainty of the measurements ($\pm 0.02 \, \mu \text{mol mol}^{-1}$). The overall increase in the bulk composition observed in the high

surface area experiment, while statistically significant, is small compared with the measured changes in (Ge/Si)_{fluid} as a function of time (Fig. 1B).

3.2. δ^{30} Si vs. Ge/Si

The co-evolution of fluid δ^{30} Si and Ge/Si for all amorphous silica precipitation experiments are plotted in Fig. 2. Starting at initial δ^{30} Si and Ge/Si values of approximately -2% and $8.45~\mu mol mol^{-1}$ respectively, δ^{30} Si $_{fluid}$ and $(Ge/Si)_{fluid}$ both increase as a function of reaction progress through the early stages of the experiments. For the medium and low surface area batches, δ^{30} Si $_{fluid}$ and $(Ge/Si)_{fluid}$ are linearly correlated $(R^2=0.86~and~R^2=0.84,$ respectively). However, as observed in the timeseries plot (Fig. 1B), a reversal is noted in the high surface area batch after ~ 1 day where fluid δ^{30} Si starts to decrease with time while $(Ge/Si)_{fluid}$ ratios continue to increase. This results in a substantial deviation from the trend between the high surface area δ^{30} Si $_{fluid}$ and $(Ge/Si)_{fluid}$ at later stages of the reaction.

4. DISCUSSION

4.1. Origin of high starting (Ge/Si)_{fluid} and potential implications of an evolving reactive surface area during dissolution

Relatively constant Ge(OH)₄ concentrations throughout the experimental duration coupled with rapid Si precipitation and elevated (Ge/Si)_{fluid} values suggest that Ge exhibits slow kinetics during amorphous silica precipitation. However, before proceeding further in this interpretation, there are two possible complications that could influence the observed data. First, we consider how accurately we know the surface area of the initial seed crystals, particularly in the high surface area experiment. As a reminder, high surface area seeds were partially dissolved at 90 °C to prepare our starting solutions before beginning the precipitation experiments. In prior amorphous silica studies that served as the basis for our experimental design (Geilert et al., 2014; Roerdink et al., 2015), this effect is minimized by using a large quantity of amorphous silica seeds for dissolution at 90 °C (10 g L⁻¹). Results from mass balance calculations indicate that only 1.65% of the total amount of amorphous silica seed initially present was dissolved in order to reach Si solubility concentrations at 90 °C (5.48 mM; Gunnarsson and Anórsson, 2000). A simplified geometric model relating mineral concentration to changes in the reactive surface area (Lichtner, 1988; Noiriel et al., 2009) suggests that this minor reduction in the solid phase should not impact the corresponding surface areas of the

$$S = S_0 \left(\frac{C}{C_0}\right)^{-2/3} \tag{4}$$

This formulation is based on a shrinking sphere model where S is the final surface area after dissolution (m^2 g^{-1}), S₀ is the starting surface area (50 m^2 g^{-1}), and C₀ and C corresponds to the amount of silica in the

Table 2
Germanium data for amorphous silica precipitation experiments.

No.	time	Si(OH) ₄ ^a	Ge(OH) ₄ ^b	N _{GeO2(ppt)} ^c	N _{GeO2(am.silica)} ^d	log R _p ^{Si a}	log R _p ^{Ge e}	(Ge/Si) _{fluid} f	(Ge/Si)pptg	(Ge/Si) _{am.silica} ^h	K _D inst i
	days	$\mu \mathbf{M}$	pM	pmoles		mole m^{-2} s ⁻¹		μ mol/mol			Bulk/fluid
High sur	face area batc	$h (50 m^2 g^{-1})$									
1	0.00	5277 ± 700	42776 ± 856		2291 ± 46			8.11 ± 0.13		0.28 ± 0.09	0.035 ± 0.006
2	0.02	5092 ± 500	42599 ± 852	52 ± 1207	2343 ± 1208	-9.48 ± 0.5	-14.9 ± 1.4	8.37 ± 0.10	2 ± 23	0.28 ± 0.52	0.034 ± 0.018
3	0.11	4600 ± 600	42855 ± 858	80 ± 1211	2371 ± 1711	-9.82 ± 0.1	-15.5 ± 1.2	9.32 ± 0.13	1 ± 15	0.28 ± 0.72	0.031 ± 0.022
4	0.19	4266 ± 700	41908 ± 838	169 ± 1199	2461 ± 2089	-9.90 ± 0.4	-15.4 ± 0.9	9.82 ± 0.16	2 ± 7	0.29 ± 0.85	0.032 ± 0.028
5	0.93	3375 ± 900	43382 ± 868	143 ± 1206	2434 ± 2413	-10.51 ± 0.5	-16.1 ± 0.9	12.85 + 0.27	1 ± 8	0.29 ± 1	0.024 ± 0.029
6	1.00	3311 ± 100	40579 ± 812	314 ± 1188	2605 ± 2689	-10.33 ± 0.6	-15.8 ± 0.6	12.25 ± 0.04	2 ± 4	0.31 ± 1.03	0.026 ± 0.027
7	2.00	2870 + 600	42451 ± 849	271 ± 1175	2562 ± 2935	-10.92 ± 0.7	-16.1 ± 0.6	14.79 ± 0.21	2 ± 4	0.30 ± 1.15	0.022 ± 0.027
8	8.87	2272 ± 200	43638 ± 873	262 ± 1218	2553 ± 3177	-11.65 ± 0.7	-16.8 ± 0.7	19.21 ± 0.09	1 ± 4	0.30 ± 1.25	0.015 ± 0.020
9	13.88	2193 ± 500	39336 ± 787	488 ± 1175	2779 ± 3387	-12.20 ± 0.7	-16.7 ± 0.4	17.93 ± 0.23	3 ± 2	0.33 ± 1.22	0.020 ± 0.025
10	18.95	2172 ± 400	39278 ± 786	530 ± 1112	2821 ± 3565	-12.49 ± 0.6	-16.8 ± 0.3	18.08 ± 0.18	3 ± 2	0.33 ± 1.26	0.019 ± 0.025
11	31.08	2051 ± 400	38855 ± 777	586 ± 1105	2877 ± 3733	-12.47 ± 0.7	-17.0 ± 0.3	18.95 ± 0.20	3 ± 2	0.34 ± 1.30	0.018 ± 0.025
seedinit										0.28 ± 0.01	
seed _{finalll}										0.33 ± 0.02	
Medium .	surface area b	oatch (0.127 m ² g	⁻¹)								
1	0.00	5334 ± 400	45631 ± 879		39982 ± 800			8.55 ± 0.08		0.56 ± 0.02	0.066 ± 0.005
2	1.83	4565 ± 400	42161 ± 843	994 ± 1243	40976 ± 1478	-8.62 ± 0.5	-13.9 ± 0.1	9.24 ± 0.09	5 ± 1	0.57 ± 0.04	0.063 ± 0.006
3	2.90	4144 ± 800	43658 ± 873	755 ± 1214	40737 ± 1912	-8.63 ± 0.6	-14.2 ± 0.2	10.53 ± 0.19	2 ± 2	0.57 ± 0.05	0.056 ± 0.013
4	4.23	3696 ± 500	43641 ± 873	890 ± 1235	40872 ± 2276	-8.70 ± 0.9	-14.3 ± 0.1	11.81 ± 0.14	2 ± 1	0.57 ± 0.06	0.049 ± 0.008
5	4.95	3618 ± 500	42024 ± 840	1406 ± 1212	41388 ± 2579	-9.04 ± 0.6	-14.2 ± 0.1	11.62 ± 0.14	3 ± 1	0.58 ± 0.06	0.051 ± 0.008
6	9.00	3219 ± 400	40454 ± 809	1901 ± 1167	41883 ± 2579	-9.23 ± 0.8	-14.3 ± 0.2	12.57 ± 0.13	3.2 ± 0.7	0.58 ± 0.07	0.048 ± 0.007
7	14.79	3091 ± 700	41350 ± 827	1815 ± 1157	41797 ± 3058	-9.80 ± 1.1	-14.6 ± 0.2	13.38 ± 0.23	2.9 ± 0.7	0.58 ± 0.07	0.046 ± 0.012
8	27.95	2948 ± 600	39346 ± 787	2397 ± 1142	42380 ± 3264	-10.13 ± 1.1	-14.7 ± 0.3	13.35 ± 0.20	3.6 ± 0.5	0.59 ± 0.08	0.046 ± 0.012
9	30.00	2955 ± 500	42548 ± 851	1792 ± 1159	41774 ± 3463	-10.09 ± 0.9	-14.8 ± 0.2	14.40 ± 0.17	2.6 ± 0.7	0.58 ± 0.08	0.042 ± 0.009
seed										0.56 ± 0.02	
Low surf	ace area batcl	$n (0.072 \text{m}^2 \text{g}^{-1})$									
1	0.00	5298 ± 500	45957 ± 919		46054 ± 921			8.7 ± 0.1		0.64 ± 0.02	0.074 ± 0.008
2	1.83	4686 ± 500	44345 ± 887	514 ± 1277	46567 ± 1575	-8.47 ± 0.2	-14.0 ± 0.4	9.46 ± 0.11	3 ± 3	0.64 ± 0.03	0.069 ± 0.008
3	2.90	4394 ± 400	49849 ± 997	-724 ± 1334	45330 ± 2064	-8.54 ± 0.3		11.34 ± 0.09	-2 ± 2	0.62 ± 0.05	0.056 ± 0.006
4	4.23	4194 ± 600	43084 ± 862	1042 ± 1318	47095 ± 2449	-8.76 ± 0.6	-14.0 ± 0.1	10.27 ± 0.14	3 ± 1	0.65 ± 0.05	0.065 ± 0.011
5	4.95	4080 ± 300	44194 ± 884	883 ± 1234	46936 ± 2742	-8.70 ± 0.5	-14.2 ± 0.1	10.83 ± 0.08	2 ± 1	0.65 ± 0.06	0.060 ± 0.006
6	9.00	3895 ± 300	45226 ± 905	748 ± 1265	46802 ± 3020	-9.28 ± 0.7	-14.5 ± 0.2	11.61 ± 0.08	2 ± 2	0.64 ± 0.06	0.056 ± 0.006
7	14.79	3817 ± 400	43839 ± 877	1187 ± 1260	47241 ± 3272	-9.72 ± 1.1	-14.49 ± 0.03	11.48 ± 0.11	3 ± 1	0.65 ± 0.07	0.057 ± 0.007
8	27.95	3618 ± 500	43555 ± 871	1363 ± 1236	47416 ± 3498	-9.77 ± 1.1	-14.71 ± 0.04	12.04 ± 0.14	2.8 ± 0.9	0.65 ± 0.07	0.055 ± 0.009
9	30.00	3610 ± 700	41984 ± 840	1833 ± 1210	47887 ± 3701	-9.70 ± 0.9	-14.6 ± 0.2	11.63 ± 0.19	3.7 ± 0.7	0.66 ± 0.08	0.059 ± 0.013
seed										0.64 ± 0.02	

^a Additional details on dissolved silica concentrations, saturation states, precipitation rates, evolving surface area, and Si stable isotope ratios can be found in Fernandez et al. (2019).

^b Measured fluid Ge concentrations with associated errors of $\pm 2\%$ RSD.

^c Cumulative mass of amorphous GeO₂ precipitated out of solution. Values determined by subtracting the picomoles Ge in solution at time, t, from initial amount in solution, at t = 0.

^d Total mass amorphous silica present in the system with associated errors calculated using error propagation.

^e Time-averaged precipitation rates for GeO₂ normalized to the surface area: $R_p^{Ge} = \frac{N_{GeO_{2(ppp)}_{IJ}} - N_{GeO_{2(ppp)}_{IJ}}}{S \cdot \Delta t_{II-I}}$ (see Eq. (5) in Fernandez et al., 2019 for further details). Uncertainty determined via standard error propagation.

f Measured fluid Ge/Si ratios where uncertainty determined using error propagation of the analytical uncertainties for Si (±5% RSD) and Ge (±2% RSD), respectively.

^g Ge/Si ratios of the cumulatively precipitated amorphous silica. Determined through mass balance calculations using the cumulative mass of amorphous GeO₂ removed ($N_{GeO2(ppt)}$) and SiO2 ($N_{SiO2(ppt)}$; Table 2 in Fernandez et al., 2019). Uncertainty calculated using standard error propagation according to sum of squares.

h Amorphous silica Ge/Si ratios were estimated by tracking the total amount of GeO_2 and SiO_2 accumulating in the growing bulk ($n_{Ge,SiO2, bulk(t=0)} + n_{Ge,SiO2, cumulative(t)}$). Uncertainty calculated via error propagation according to the sum of squares using both the analytical error for the initial seeds and measured fluid Ge and Si uncertainties.

ⁱ The instantaneous partition coefficient calculated as $\frac{(Ge/Si)_{om,silica}}{(Ge/Si)_{nuid}}$, monitored throughout the course of the reaction for an evolving bulk solid phase. Error determined using Monte Carlo.

amorphous phase present prior to and after dissolution (µmoles). The calculation indicates an insignificant change in surface area ($\approx 0.002\%$). Furthermore, this calculation reminds us that dissolution would increase the specific surface area of the remaining seeds, thus speeding up the reaction and presumably allowing more Ge incorporation into the growing solid. Although a simplified approach, Eq. (4) supports the assumptions of Roerdink et al. (2015) and Fernandez et al. (2019) and we proceed with the understanding that that changes to the surface area are not sufficient to affect our precipitation rates or the estimation of $^{\text{Ge}}$ k (Eq. (2), Section 2.3).

Second, we consider the potential for heterogeneity in the Ge content of the initial amorphous silica seeds. If the initially elevated (Ge/Si)_{fluid} values were caused by dissolution of a Ge-enriched rim coating our seed crystals, then rapid re-equilibration with this Ge-enriched surface layer could sustain high (Ge/Si)fluid values throughout the duration of the experiment. However, several lines of evidence refute this option as a likely explanation. To start, the likelihood of amorphous silica seeds becoming strongly zoned during the fabrication process is quite low. Assuming a zoned version of our high surface area seeds where the outermost surface has a Ge/Si ratio of $\sim 8.45 \,\mu\text{mol mol}^{-1}$, mass balance calculations suggest that approximately 50% of the total Ge present in the solid would need to be concentrated in the upper 0.32 nm of an individual grain perpendicular to its surface. This is smaller than the size of a unit cell in an SiO₂ crystal structure (0.5405 nm for α quartz; Ackermann and Sorrel, 1974; Wright and Lehmann, 1981). Finally, high (Ge/Si)_{fluid} values with respect to the dissolving mineral assemblage (0.2-2.5 µmol mol⁻¹) are systematically observed at elevated temperatures with values ranging from

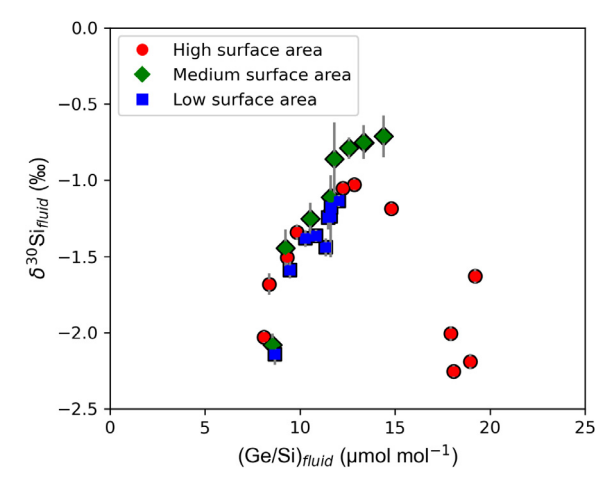


Fig. 2. Fluid δ^{30} Si as a function of Ge/Si ratio for the high (red circles), medium (green diamonds), and low (blue squares) surface area batches. Starting values are the points on the far left of the graph. A parabolic-type relationship characterizes the δ^{30} Si and Ge/Si variability in the high surface area batch, which represents fast δ^{30} Si re-equilibration relative to the rates of Ge/Si equilibrium partitioning (that are negligible over this experimental timespan). Error bars represent 2 standard deviation for the Si stable isotope data (Fernandez et al., 2019) and 2% and 5% RSD for Ge and Si concentration measurements used in Ge/Si calculations. (For interpretation of the references to colour in this figure legend, the reader is referred to the web version of this article.)

1000 μmol mol⁻¹ (Arnórsson, 1984; Pokrovski and Schott, 1998; Evans and Derry, 2002; Pokrovski et al., 2005; Escoube et al., 2015). Increasing (Ge/Si)_{fluid} with increasing temperature can be attributed to preferential partitioning of Ge with respect to Si arising from differences

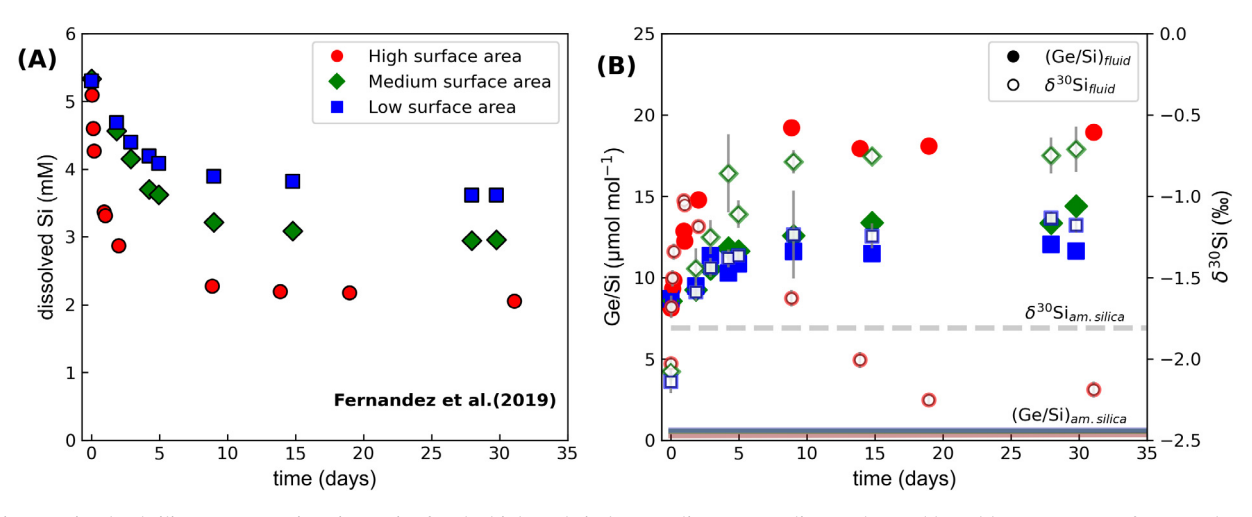


Fig. 1. Dissolved silica concentration timeseries for the high (red circles), medium (green diamonds), and low (blue squares) surface area batch experiments (**A**) from Fernandez et al. (2019) and (**B**) corresponding measured fluid δ^{30} Si (open markers, Fernandez et al., 2019) and Ge/Si ratios (solid markers, this study) as a function of time for the \sim 30-day experiments. Error bars correspond to 2 standard deviations for the Si stable isotope measurements. Ge/Si analytical uncertainty is within the marker sizes and correspond to 2% and 5% RSD for Ge and Si concentration measurements, respectively. Initial Ge/Si composition of the bulk phase is represented by the grey bar and red, green, and blue lines correspond to the evolving Ge/Si amorphous silica composition with time (see Table 2). Fluid Ge/Si ratios remain elevated with respect to the compositions of the high (0.28 \pm 0.01 μ mol mol⁻¹), medium (0.56 \pm 0.02 μ mol mol⁻¹), and low (0.64 \pm 0.02 μ mol mol⁻¹) surface area seed crystals. (For interpretation of the references to colour in this figure legend, the reader is referred to the web version of this article.)

in the thermodynamic properties of Ge(OH)_{4(aq)} and Si (OH)_{4(aq)} (Pokrovski and Schott, 1998; Pokrovski et al., 2005). This high temperature effect is not observed at ambient conditions characteristic of natural terrestrial weathering and marine environments where (Ge/Si)_{fluid} reflects the composition of the dissolving silicate rocks (Kurtz et al., 2002) and diatoms (Froelich et al., 1984, 1992; Mortlock et al., 1991), respectively. However, our starting (Ge/Si)_{fluid} are consistent with a preferential Ge partitioning during the pre-dissolution step at 90 °C.

Regardless, even if the seeds were initially zoned, subsequent rapid re-equilibration with a Ge-enriched outer surface throughout the extent of the reaction is not possible. Mass balance calculations show that $\sim 70\%$ of the total Si lost from solution takes place over the first day, resulting in the formation of a strongly depleted Ge mineral surface that would effectively isolate the zoned interior from the fluid. Thus, the fluid would only be interacting and reequilibrating with the recently-formed mineral surface and a strongly heterogeneous solid interior would have no effect on the overall (Ge/Si)_{fluid}.

Having ruled out these complicating effects, we conclude that Ge precipitation kinetics are slow relative to Si. This offers the simplest and most plausible explanation for our experimental results. However, in natural settings, it is observed that Ge is (eventually) incorporated into secondary silicates. To determine how slow Ge incorporation is during amorphous silica formation, we now turn to the application of our trace model under the assumption that our previous stable isotope fractionation framework (Fernandez et al., 2019) also describes the partitioning of this trace element.

4.2. Trace model: Ge exchange under a stable isotope fractionation framework

Observed fluid Ge/Si behavior during the amorphous silica growth experiments is interpreted through a series of numerical simulations adapting the CrunchTope silicon isotope fractionation model reported in our prior study (Fernandez et al., 2019) to a trace element. Initial conditions for these numerical experiments are summarized in Table 3. Silica kinetic and thermodynamic parameters for all simulations were kept constant with a log kinetic rate and equilibrium constant of -9.67 (Rimstidt and Barnes, 1980) and -2.7135 (Gunnarsson and Anórsson, 2000), respectively (Table 3). Potential factors that could influence amorphous silica solubility concentrations and kinetic rates such as temperature and pH were minimized via the experimental design. Further, the impact of the surface area and its evolution during mineral growth on amorphous silica solubility was rigorously examined by Fernandez et al. (2019) using the Freundlich-Ostwald equation (Enüston and Turkevich, 1960), finding no significant changes in the solubility across the three surface area conditions.

The equilibrium K_D imposed ($D_{\rm eq}=0.08$, Table 3) derives from our estimated value based on a quartz–argutite ideal solid solution (further details provided in Section 2.3). The kinetic rate constant for the incorporation of dissolved Ge in the solid as ${\rm GeO}_{2(am)}$ was estimated by

Table 3
Initial conditions for the Ge, trace element batch model.

Parameters	Units	Conservative	Ge incorporation
Reaction order (m)		3.5	3.5
Duration (short)	days	35	35
Duration (long)	years		1 - 1000
Max Timestep	hours	9.6	9.6
T	°C	25	25
pН		7.33	7.33
Specific surface area	$m^2 g^{-1}$	50 (high)	50 (high)
		0.127	0.127
		(medium)	(medium)
		0.072 (low)	0.072 (low)
Si(OH) _{4(aq)} ^a	mM	5.277	5.277
$Ge(OH)_{4(aq)}^{b}$	mM	4.2776×10^{-5}	4.2776×10^{-5}
log Sikc		-9.67	-9.67
log Gek,d		-	-19.7
log SiKege		-2.7135	-2.7135
log GeKeq f		-	-3.8198
(Ge/Si) _{fluid}	μmol mol ⁻¹	8.11	8.11
(Ge/Si) _{am.silica}	μmol	0.28 (high)	0.28 (high)
	mol^{-1}	0.56 (medium)	0.56 (medium)
		0.64 (low)	0.64 (low)
D_{EO}^g		-	0.08
Dkin		-	9.3×10^{-11}

^a Measured starting dissolved Si concentrations from Fernandez et al. (2019).

an optimization approach where the Ge kinetic rate parameter (log Gek; Table 3) was altered across a suite of numerical simulations (while keeping GeK_{eq} and all other parameters fixed) until an optimal value was found which provided the "best fit" to our fluid Ge concentration data (Fig. 3). The range of kinetic Ge rate constants tested spanned roughly 6 orders of magnitude from a maximum rate of $10^{-12.6}$ mol m⁻² s⁻¹ (~3 orders of magnitude slower than Si) to a minimum rate of $10^{-26.7}$ mol m⁻² s⁻¹ (~17 orders of magnitude slower than Si). Our optimized Ge rate constant value was determined to be $10^{-19.7 \pm 1.1}$ mol m⁻² s⁻¹, approximately 10 orders of magnitude slower than the Si kinetic rate constant ($10^{-9.67}$ mol m⁻² s⁻¹; Rimstidt and Barnes, 1980). This yields a kinetic fractionation factor, D_{kin} (Gek/Sik), of 9.33 × 10⁻¹¹. A Monte-Carlo sensitivity analysis performed over a broad kinetic and equilibrium K_D parameter space further supports our combined estimates for ^{Ge}K_{eq} and ^{Ge}k (Appendix A).

b Measured starting dissolved Ge concentrations from this study.

^c Rimstidt and Barnes (1980).

^d Determined through taking a best fit of the experimental fluid Ge/Si data.

^e Gunnarsson and Anórsson (2000).

^f Estimated using Evans and Derry (2002) equilibrium model for germanium bearing quartz (Section 2.3, Eq. (3)).

g Equilibrium partition coefficient (D_{EQ}) calculated as the ratio between $GeO_{2(am)}$ and $SiO_{2(am)}$ equilibrium constants, $\frac{K_{eq,GeO_2}}{K_{eq,SiO_2}}$.

^h Kinetic partition coefficient calculated as the ratio between $GeO_{2(am)}$ and $SiO_{2(am)}$ precipitation rate constants: $\frac{Ge_k}{Si_k}$.

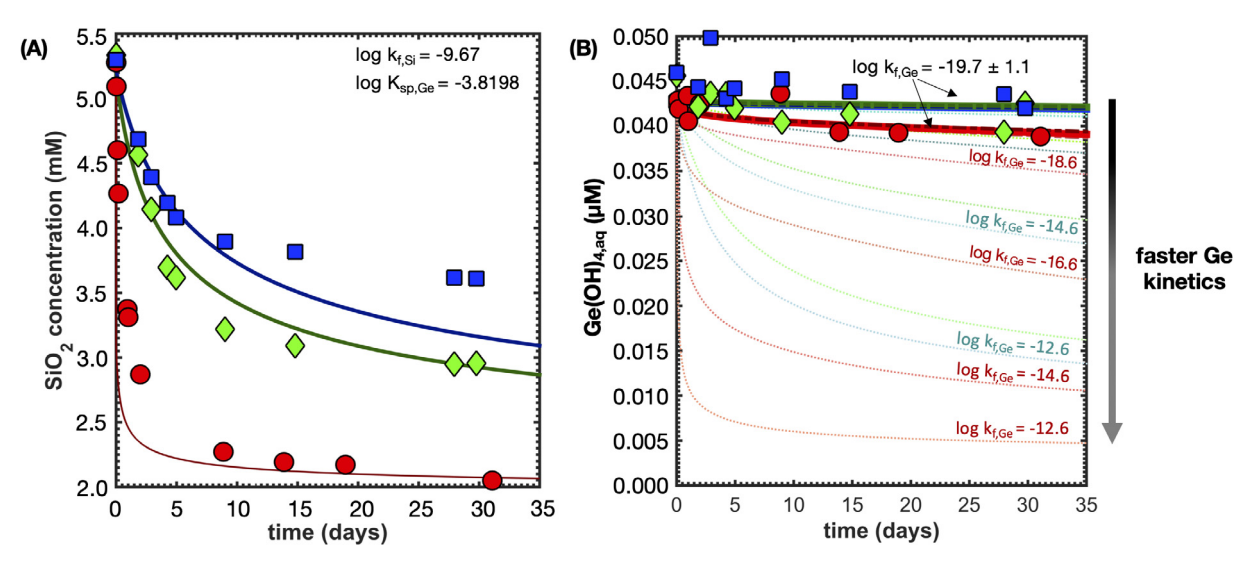


Fig. 3. Fluid silicon (A) and germanium (B) concentrations as a function of the experimental duration (\sim 35 days). Ge kinetic rate constant (log ^{Ge}k) was determined based on a "best-fit" approach of the three mass exchange models (Section 4.2) to the experimental data for a given Ge equilibrium constant ($^{Ge}K_{eq} = 10^{-3.8198}$) calculated based on an equilibrium thermodynamic model assuming ideal solid–state solution (Eq. (3)) between quartz (SiO₂) and arguite (GeO₂). The range of Ge kinetic rate constants tested spanned roughly 7 orders of magnitude from $10^{-12.6}$ to $10^{-19.8}$ mol m⁻² s⁻¹. Errors are 2% and 5% RSD for Ge and Si concentration measurements used in Ge/Si calculations.

Flexibility in defining the component of the mineral that contributes to the mole fraction (X) within the Ge trace model (Section 2.3, Eq. (2)) allows us to test several possible Ge fluid-mineral mass exchange processes that could describe our observed Ge/Si partitioning. Three Ge fluidmineral exchange approaches (Druhan et al., 2013) were explored in the model, designated respectively as (1) "noback reaction", (2) "bulk", and (3) "surface". In the "no back reaction" scenario, X is set to the aqueous mole fraction, which decouples Ge and Si from each other (i.e. the precipitation rate is decoupled from the molar fraction in the solid) and, thus, only a kinetic fractionation is imposed in the model (Dkin). In this context, Ge and Si evolve irreversibly and the observed K_D reflects their individual evolutions along their respective, unidirectional reaction pathways. In the "bulk" and "surface" exchange scenarios the fluid and solid phases are allowed to equilibrate with one another by defining X in terms of the solid mole fraction. Thus, D_{EQ} is imposed in these scenarios as opposed to the "no back reaction" case. The most straightforward approach is to allow the fluid to interact with the total solid or "bulk" composition through time. However, this "bulk" approach ignores the potentially significant impact of an evolving or zoning mineral surface on observed fluid variability during "free-drift" mineral growth. Thus, a "surface" approach was developed in an attempt to address this effect by allowing the fluid to interact with only the portion of the mineral that has been most recently formed (Druhan et al., 2013; Steefel et al., 2014; Fernandez et al., 2019). In this scenario, the depth into the mineral surface in contact with the fluid (i.e., the fluid-mineral interaction depth) is approximated through a running average of the composition of the mass recently precipitated out of the fluid over a user-defined number of timesteps (details regarding this numerical implementation can be found in Druhan et al., 2013; Fernandez et al., 2019). This scenario

implies that the fluid–solid interaction depth varies as a function of reaction progress. This varying fluid–solid interaction depth is an assumed underlying process which Fernandez et al. (2019) successfully used to create a forward model of contemporaneous mineral surface and fluid δ^{30} Si evolution through time. Thus, we now extend this approach to the complementary Ge/Si system.

4.3. Ge partitioning over experimental timescales

The Ge trace model (Eq. (2)) generally reproduces our measured fluid Ge/Si evolution through time across the various surface area conditions (Fig. 4A). However, (Ge/Si)_{fluid} appears to be less sensitive to the different mass exchange scenarios ("no back reaction", "bulk", and "surface") over the experimental duration compared to the contemporaneous Si stable isotope ratios (Fig. 4B). This is particularly apparent in the low and medium surface area cases in which net reaction rates are too slow to distinguish between these three Ge mass exchange scenarios. The faster kinetics and subsequent re-equilibration of the high surface area case create a greater response in the (Ge/Si)_{fluid} over the 1-month experimental timescale. Thus, Ge is shown to exhibit quasi-conservative behavior during early (kinetically dominated) stages of amorphous silica growth.

The most promising case for extracting information relevant to Ge incorporation and the fluid–mineral exchange mechanism underlying observed Ge partitioning lies in the high surface area experiment. In this case, the system evolved at fast enough rates to capture the beginning of non-conservative behavior as evidenced by overall greater sensitivity to the different fluid–mineral mass exchange scenarios (Fig. 4A). Application of a "no-back reaction" model to the measured high surface area (Ge/Si)_{fluid} over-predicts the extent of kinetic partitioning (in a manner comparable to that observed for δ^{30} Si, Fig. 4B). The numerical

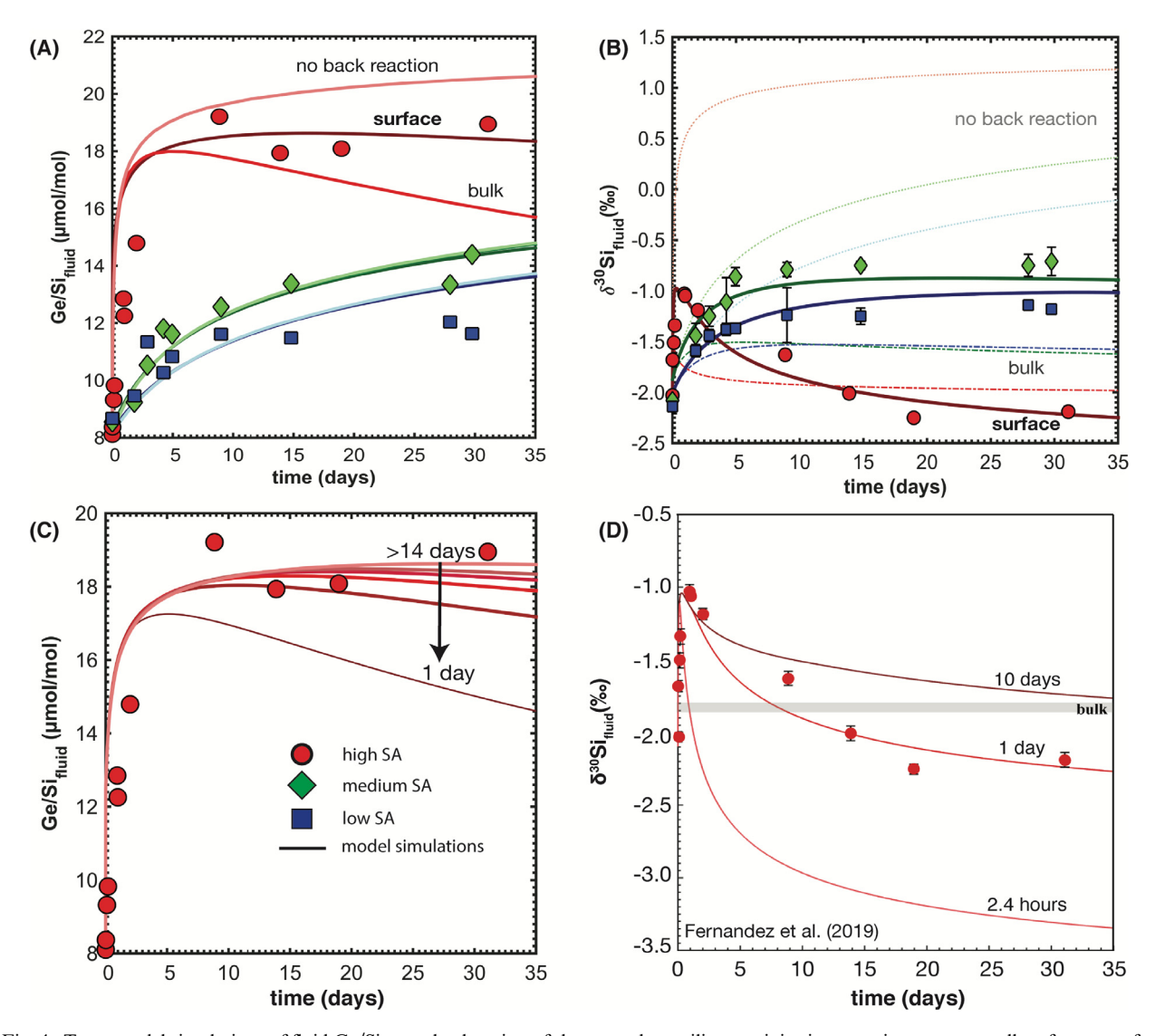


Fig. 4. Trace model simulations of fluid Ge/Si over the duration of the amorphous silica precipitation experiments across all surface areas for the three "no back reaction", "bulk", and "surface" mass exchange scenarios (A). Fluid Ge/Si simulations are compared to previous simulations performed across the same exchange scenarios for fluid δ^{30} Si (B) reported in Fernandez et al. (2019). Fluid δ^{30} Si show higher sensitivity to the different approaches in which the fluid can interact with the growing amorphous silica phase. The "surface" approach provides the best fit to the high surface area Ge/Si and δ^{30} Si. However, the time intervals (or fluid–mineral interaction depths) determined based on sensitivity analyses for Ge/Si and δ^{30} Si are distinct, >14 days (C) and 1 day (D), respectively. Error bars correspond to \pm 2 SD for Si stable isotopes (C, D). Analytical uncertainty for Ge/Si measurements correspond to 1–3% RSD and are within the bounds of the symbols.

simulation involving fluid equilibration with the "bulk" mineral also fails to capture experimental $(Ge/Si)_{fluid}$ behavior. In this situation, fluid interaction with the total seed composition $(0.28 \, \mu \text{mol mol}^{-1})$ predicts a faster decrease in $(Ge/Si)_{fluid}$ to values lower than observed in the experiment.

For both Ge/Si and δ^{30} Si, the "surface" exchange scenario involving fluid interaction with a co-evolving mineral surface offers the most accurate representation of the high surface area data. The optimal number of timesteps to average over (i.e., the proxy for the fluid–mineral interaction depth or the portion of the recently-formed mineral surface in contact with the fluid) was identified through the same

sensitivity analysis performed for δ^{30} Si (Fig. 4C, D; Fernandez et al., 2019). This sensitivity analysis yielded a surface equilibration time interval of > 14 days for the high surface area experimental Ge/Si data (Fig. 4C), distinctly larger than that determined for δ^{30} Si (1 day, Fig. 4D; Fernandez et al., 2019). The total mass of newly formed precipitate generated on the high surface area seeds was estimated to correspond to a depth of 0.19 nm (Fernandez et al., 2019). For the δ^{30} Si study, a time interval of 1 day implies fast kinetics and fluid interaction with only a very thin portion of the mineral surface (\sim 0.09 nm, Fernandez et al., 2019). Hence, for the same net amorphous silica formation rates, a longer time interval (or a greater

fluid-mineral surface interaction depth) for Ge/Si implies slower overall kinetics and a relatively longer approach to equilibrium.

Therefore, differences in observed fluid δ^{30} Si and Ge/Si behavior throughout the extent of the reaction can be interpreted from a "surface" exchange perspective. For δ^{30} Si, faster kinetics and a smaller fluid-mineral surface interaction depth ultimately drives high surface area δ³⁰Si_{fluid} to values more negative than the bulk mineral phase (-1.81) $\pm 0.03\%$), reflective of the fluid interacting with a strongly ³⁰Si-depleted mineral surface composition. On the other hand, slower Ge kinetics and a larger fluid-mineral surface interaction depth results in (Ge/Si)fluid remaining at elevated values throughout the experimental duration. Quick precipitation of amorphous silica compared to relatively sluggish Ge incorporation results in the fluid interacting with a highly depleted Ge/Si mineral surface (Appendix B, Fig. B.1). Up to 70% of the total Si precipitated out of solution is generated during the first day of the experiment. Fluid interaction with this initially low mineral surface Ge/ Si composition shifts (Ge/Si)_{fluid} to values lower than would be predicted in a "no-back reaction" mass exchange scenario. Due to the relatively small amount of mass precipitated compared to the total mass of amorphous silica present in the system, the mineral surface is highly sensitive to any minor incorporation of Ge. Thus, the surface composition is predicted in the model to increase with time to higher Ge/Si ratios $((Ge/Si)_{pot} = 2.81 \, \mu mol \, mol^{-1})$ in agreement with simple mass balance approximations using the experimental data (Table 2). The ability of the "surface" option to better predict high surface area data supports a mass exchange between the fluid and mineral surface as the principal driver of observed (Ge/Si)_{fluid}. Further, a major finding from these numerical simulations is that Ge/Si and δ^{30} Si have different equilibration timescales and, thus, represent two distinct "clocks". In this regard, Ge/Si may serve as a potent (near)equilibrium tracer in a manner similar to the ²⁹Si equilibrium tracer (Zheng et al., 2019; Zhu et al., 2020).

This result implies quite distinct kinetic behavior between Ge and Si where Ge kinetic partitioning is notably slower. Therefore, substantial residence times or path lengths would be necessary to observe Ge incorporation into secondary phases in natural settings. At first glance this may appear to contradict a recent study by Perez-Fodich and Derry, 2020, who used a CrunchTope framework to model Ge/Si incorporation into kaolinite based on field observations. They suggested that overall fast precipitation rates of kaolinite and comparable Ge and Si kinetics were necessary to explain observed ratios in weathering environments. However, it should be clarified that Perez-Fodich and Derry (2020) did not directly model kinetic Ge partitioning during the growth of kaolinite. Rather, they simply note that if kaolinite growth is slow, Ge incorporation is slow and thus the fluid Ge/Si ratio remains elevated. Our results are the first to directly illustrate Ge incorporation into secondary minerals during growth, and clearly show that Ge kinetics are slow relative to Si. This present study utilizes amorphous SiO₂, but the results open the possibility that slow Ge kinetics may also exists for aluminosilicate clays. These findings suggest that the transport timescales in natural systems may require re-evaluation in light of the unique behavior of Ge kinetics relative to Si during amorphous silica formation using a direct simulation of Ge kinetics in the modeling framework presented here.

Taking these simulations as a guide, we can now address a driving question in this study: Is a rate-dependent fractionation framework sufficient to capture both Ge/Si and Si stable isotope behavior simultaneously in the same system? The answer is a conditional "yes". The data-model comparison offers substantial evidence to suggest Ge/Si and $\delta^{30}\text{Si}$ are self-consistent during amorphous silica formation. However, this is predicated on the idea that Ge in the fluid phase interacts with a very different component of the newly formed amorphous silica surface than its fluid $\delta^{30}\text{Si}$ counterpart. These findings have significant implications for how the observed K_D is defined and interpreted when we extend out to longer timescales.

4.4. Forecasting Ge behavior over long timescales

This section uses the Ge trace model to forecast Ge behavior at longer (annual to millennial) timescales based on our range of precipitation rates and mineral surface areas. Since no data are available at these timescales for amorphous silica precipitation to validate the model predictions, these results should be regarded as hypotheses that we present as a driver for future research in Ge/Si partitioning during secondary silicate formation. The trace model was run out to 1000 years for all three surface areas, capturing timescales that can be observed in a wide range of natural system. Only the bulk and surface fluid—mineral exchange scenarios are used for these simulations as the no back-reaction model will never allow dissolved Ge to re-equilibrate with the solid phase.

Overall, we observe a general trend where the observed partition coefficient, K_D ((Ge/Si)_{solid}/(Ge/Si)_{fluid} where $solid = bulk \ \ (Ge/Si)_{am.silica} \ \ or \ \ cumulatively \ \ precipitated$ (Ge/Si)ppt amorphous silica) increases over longer timescales as Ge incorporation is allowed to proceed (Fig. 5). This result corresponds with an associated decrease in modeled (Ge/Si)_{fluid} to lower values as a function of time (~1.2 $\pm 0.2 \,\mu\text{mol mol}^{-1}$ for the high surface area case, Appendix C). The extent of Ge incorporation into the solid is strongly dependent on the rate at which equilibrium is approached, which is coupled to the surface area. Importantly, overall amorphous silica precipitation at these timescales is extremely slow and the system is functioning at (near) equilibrium conditions. Thus, equilibrium exchange is driving observed Ge/Si behavior. Despite the obvious limitations in our ability to independently validate such forecasted Ge/Si partitioning over these timescales, our results consistently demonstrate that Ge does eventually become incorporated into amorphous silica. Therefore, the general observation of higher Ge/Si ratios in the solid phase during secondary mineral formation is eventually recovered in our models at longer annual to decadal timescales.

On the experimental timescale, fluid phase δ^{30} Si and Ge/Si were found to be positively correlated, increasing during early stages of amorphous silica growth. This observation

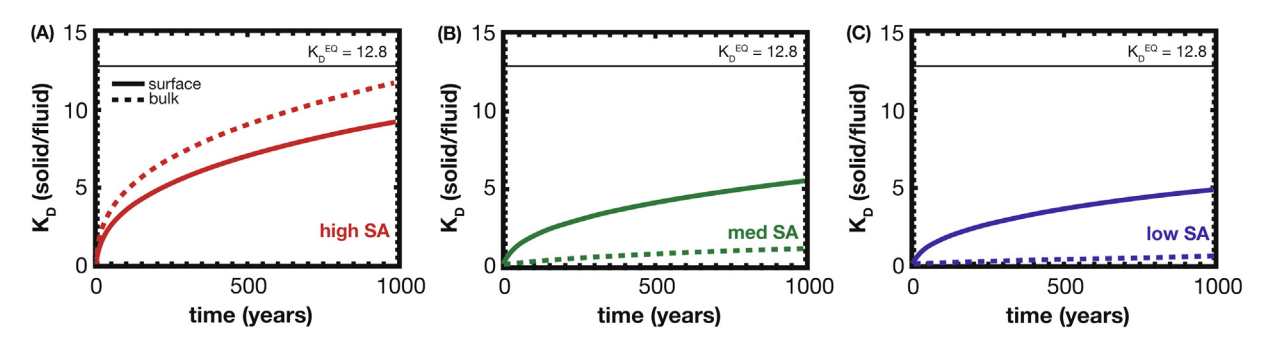


Fig. 5. Long-term model simulations for the evolution of the observed Ge partition coefficient, K_D , over 1000 years for the high (A), medium (B), and low (C) surface area conditions. Predictions from the two different fluid–mineral equilibration scenarios; "bulk" (dashed line) and "surface" (solid line) are shown alongside the predicted equilibrium partition coefficient, K_D^{EQ} , equal to 12.8 (Eq. (3)). In all cases, observed K_D behavior suggest that Ge partitioning is still far from equilibrium conditions at the end of the simulation.

goes against the inverse relationship between the two tracers that has been previously documented in the literature for secondary clay formation in field settings (Cornelis et al., 2010; Opfergelt et al., 2010; Delvigne et al., 2016). There are potentially several reasons for this discrepancy. Secondary clay formation rates are characteristically slow, as for kaolinite, which has a precipitation rate that is roughly four orders of magnitude slower than amorphous silica ($10^{-13.6}$ mol m⁻² s⁻¹; Yang and Steefel, 2008). At slow enough precipitation rates, it could be possible that Ge incorporation occurs at comparable timescales to δ^{30} Si fractionation and, thus, generates the inverse relationship commonly observed. Results from our long-term Ge trace model predictions suggest an alternative explanation for this discrepancy, which is linked to the extent of reactivity in the system and large differences in δ^{30} Si and Ge/Si equilibration timescales. Field observations could potentially be biased towards equilibrated systems where observed increases in secondary phase Ge/Si ratios, such as those reported during storm events in the Rio Icacos watershed in Puerto Rico (Kurtz et al., 2011), may reflect late-stage mineral recrystallization conditions. However, as we will discuss further in Section 4.7, an alternative explanation for such field observations could be associated with faster Ge uptake reactions such as adsorption and coprecipitation onto iron hydroxides (Pokrovsky et al., 2006).

Finally, results from the Ge trace model highlight the importance of Ge equilibrium partitioning, which ultimately dominates the long-term evolution of fluid Ge/Si signatures. Substantial evidence from both our experiments and model runs point to the role of the mineral surface area in dictating the extent of reaction progress and associated Ge/Si partitioning during amorphous silica precipitation onto pre-existing seeds. In other words, high surface areas (>1 m² g⁻¹) "accelerate" whereas lower surface areas (<1 m² g⁻¹) act as "brakes" on the extent of Ge/Si partitioning. Despite the relatively sluggish Ge incorporation rates observed in the experiments, we predict that fluid Ge/Si ratios will eventually shift to lower values typically observed in natural waters ($\sim 0.6 \pm 0.06 \,\mu\text{mol mol}^{-1}$; Mortlock and Froelich, 1987). The time that it will take to reach naturally observed Ge/Si ratios is only approximated in our long-timescale simulations, but our results do appear to overlap with the average fluid residence times of groundwaters (<50 years old, Gleeson et al., 2015) and deep marine sediment porewaters (Bard et al., 1989; Tréguer et al., 1995). From these simulations, Ge/Si partitioning timescales are found to be strongly lagged compared to δ^{30} Si fractionation in that Ge incorporation occurs at (near)equilibrium conditions. In other words, despite the capability of both systems to express unique kinetic and equilibrium effects, the timescales over which kinetic signatures are erased after reaching chemical equilibrium are predicted to be quite different for Ge/Si and δ^{30} Si.

4.5. The instantaneous partition coefficient, K_D^{inst} and observed rate dependence

4.5.1. Defining the instantaneous partition coefficient

Even under "chemostatic" conditions where mineral growth occurs under fixed saturation states and solute compositions, heterogeneity in the growing mineral surface has been observed for Sr/Ca during calcite precipitation (Tang et al., 2008). In the calcite literature, the effect of this mineral zoning on the instantaneous partition coefficient was accounted for by recasting the traditional method of calculating the partition coefficient (Eq. (5a)) in terms of a Rayleigh distillation type evolution in the bulk as shown below (Eq. (5b)):

$$K_{D}^{\text{inst}} = \frac{(\text{Ge/Si})_{\text{am.silica}}}{(\text{Ge/Si})_{\text{aq}}}$$
 (5a)

$$\left(\frac{Ge}{Si}\right)_{\text{am.silica}} = \left(\frac{Ge}{Si}\right)_{\text{fluid},0} \times \frac{1 - \left(\frac{Si}{Si_0}\right)_{\text{fluid}}^{K_{\text{inst}}^{\text{inst}}}}{1 - \left(\frac{Si}{Si_0}\right)_{\text{fluid}}} \tag{5b}$$

Here these two approaches to calculating K_D^{inst} are modified from the Tang et al. (2008) study to apply to our Ge/Si data for amorphous silica precipitation. In Eq. (5b), $\left(\frac{Ge}{Si}\right)_{fluid,0}$ represents the initial fluid Ge/Si ratio, while $\left(\frac{Si}{Si_0}\right)_{fluid}$ represents the fraction of Si remaining in solution (Si = concentration of dissolved Si at time t, Si_{0,aq} = initial SiO_{2(aq)} concentration), and $\left(\frac{Ge}{Si}\right)_{am.silica}$ represents a running estimate of bulk amorphous silica composition through time (Table 2). Eq. (5b) can then be rearranged to solve for the K_D^{inst} at each sample interval (Appendix D). Our

experiments incorporate the additional complexity of "free-drifting" conditions, such that the instantaneous partition coefficient (K_D^{inst}) for Ge may be strongly influenced by heterogeneity in the growing mineral surface. To encapsulate all of these considerations in the calculation of K_D^{inst} , we adopt two distinct estimates (Eq. (5a) and Eq. (5b)) across all three surface areas.

These approaches to calculating K_D^{inst} yield distinct values for each surface area tested, implying that the partition coefficient appears to be rate dependent (Fig. 6). All calculated partition coefficients are $\ll 1$, reflecting the artificially high starting fluid Ge/Si ratios that are caused by an initial (Ge/Si)_{fluid} that is much higher than the initial ratio of the seed crystals. K_D^{inst} does not seem to be significantly influenced by the co-evolution of the fluid and bulk solid Ge/ Si ratio during amorphous silica growth. In all cases, the differences between the two calculated partition coefficients increase with decreasing precipitation rates. Similar observations for a rate dependent K_D^{inst} have been reported in the carbonate literature for Sr trace element partitioning during calcium carbonate formation (Lorens, 1981; Tesoriero and Pankow, 1996; Huang and Fairchild, 2001; Nehrke et al., 2007; Tang et al., 2008, 2012; Böhm et al., 2012; Gabitov et al., 2014; AlKhatib and Eisenhauer, 2017). Rate dependence in these studies were interpreted to reflect greater incorporation of the trace element into the growing solid at faster precipitation rates. However, based on information from Ge trace model results at both experimental and longer timescales, the observed rate dependence cannot be interpreted in the same manner.

4.5.2. K_D^{inst} rate dependent behavior for equilibrium tracers

For the purpose of this discussion and to allow for these results to be extended to other systems, our low experimental K_D^{inst} values determined in Section 4.5.1 were renormalized to reflect a starting (Ge/Si)_{fluid} equal to the bulk solid

phase composition (0.28–0.64 µmol mol $^{-1}$). For the experimentally determined values, K_D^{inst} were normalized by applying the difference between the initial measured fluid and bulk Ge/Si ratios (i.e. $(Ge/Si)_{fluid,init} - (Ge/Si)_{am.silica,init}$) to the rest of the measured $(Ge/Si)_{fluid,init} - (Ge/Si)_{am.silica,init}$) to the rest of the measured $(Ge/Si)_{fluid,init} - (Ge/Si)_{am.silica,init}$) to the rest of the measured $(Ge/Si)_{fluid}$ values as a function of time. Normalization of numerically estimated K_D^{inst} values was invoked in the Ge trace model by setting $(Ge/Si)_{fluid}$ equal to that of the bulk in the initial conditions and then running the model out to identical short (35 days) and long (1000 year) times under a "surface" mass exchange scenario. This renormalization approach is justifiable considering that the Ge trace model successfully captures observed $(Ge/Si)_{fluid}$ variability over the experimental duration (Fig. 4A).

Results of normalized K_D^{inst} (denoted from here on as K_{D}^{*}) are shown in Fig. 7 as a function of the amorphous silica precipitation rate (R_p) using both the bulk (Fig. 7A) and cumulatively precipitated (Fig. 7B) solid compositions over longer timescales. Over the experimental duration, observed K_D^* is shown to decrease as R_p decreases for all surface area conditions (Fig. 7C). However, the relationship between K_D* and R_p eventually flips as we extend farther into (near)equilibrium conditions during late-stage mineral growth, reflecting a transition from kinetic to equilibrium partitioning regimes. In the kinetic regime, quasiconservative Ge behavior coupled to active silica precipitation results in a newly formed solid Ge/Si that is initially Ge-depleted, resulting in a decrease in K_D^* as a function of R_p (Fig. 7C). Although Ge shows similar rate dependence to those seen in other trace elements (notably Sr during carbonate formation), the factors underlying this observed correlation between KD* and Rp are quite distinct. For the trace element Sr, observed decreases in K_D^{inst} as a function of the net precipitation rate reflect uptake rates that are fast enough to "keep up" with carbonate formation (Wasylenki et al., 2005; Gabitov and Watson, 2006;

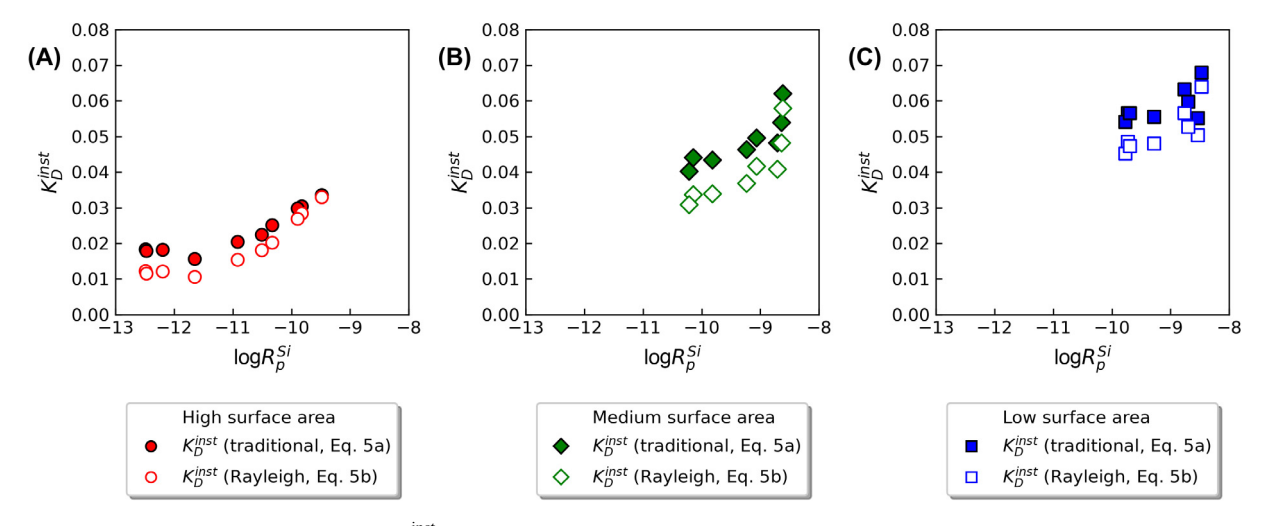


Fig. 6. Instantaneous partition coefficient, K_D^{inst} , as a function of experimentally determined silica precipitation rates (presented here in log units; Fernandez et al., 2019) for the high (A), medium (B), and low (C) surface area amorphous silica precipitation batch experiments. The different K_D trends represent different methods of calculating the partition coefficient. To account for the evolving bulk amorphous silica composition with time in these "free-drifting" experiments, K_D^{inst} can be calculated either through the traditional method (Eq. (5a)) or through a modified Rayleigh distillation approach (Eq. (5b), Tang et al., 2008).

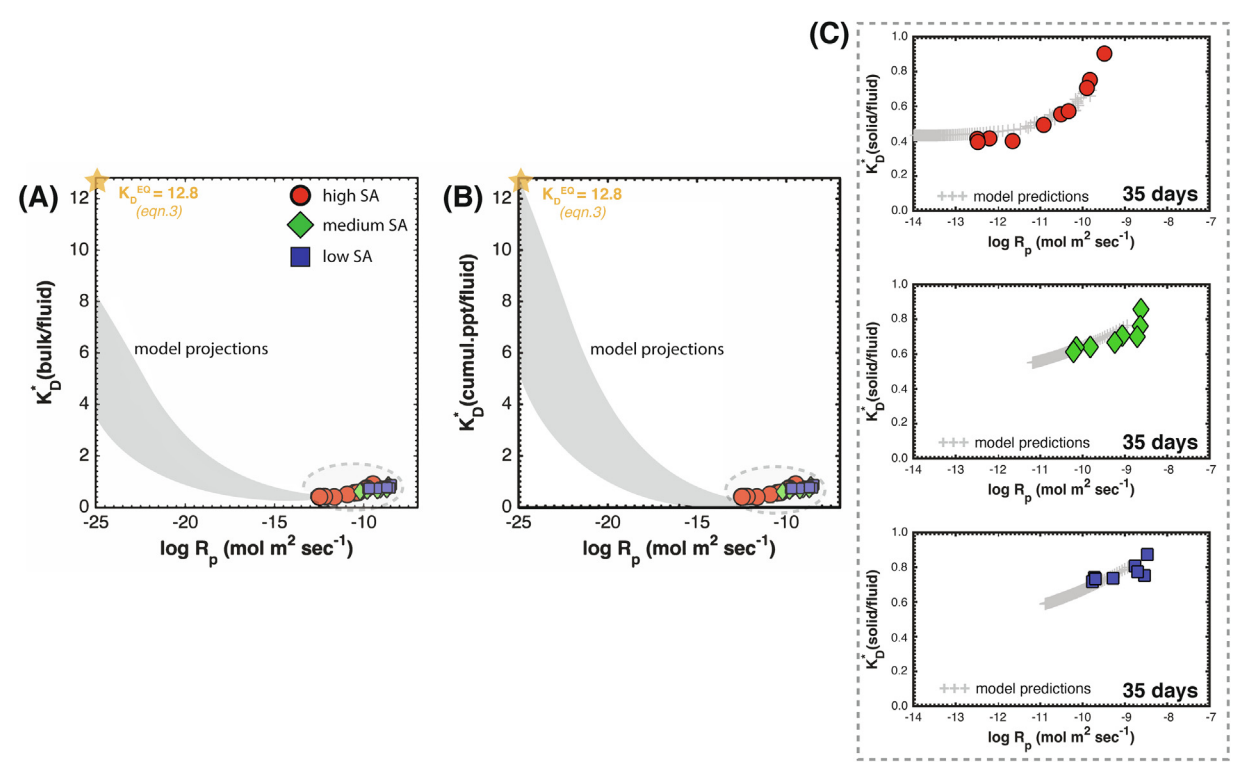


Fig. 7. Normalized K_D^{inst} (K_D^* , $Ge/Si_{fluid} = Ge/Si_{solid}$) as a function of silica precipitation rates (log R_p) for long term simulations (1000 years). K_D^* can be calculated using the "bulk" or total solid (A) or cumulatively precipitated (B) composition. The predicted instantaneous partition coefficient at equilibrium, K_D equal to ~ 12.8 (Eq. (3)), is represented by a yellow star. High, medium, and low surface area experimental data (~ 35 days) are shown as solid markers whereas numerical predictions are depicted as shaded gray areas. Mass balance and model predictions performed using the "surface" fluid-mineral mass exchange scenario are parsed out for each given surface area (C). At early times, K_D^* is observed to decrease with decreasing precipitation rates as a result of quasi-conservative Ge behavior during the beginning of amorphous silica growth. At (near) equilibrium conditions, the relationship between K_D and R_p flips from a positive to an inverse correlation where K_D increases with decreasing R_p .

Tang et al., 2008; AlKhatib and Eisenhauer, 2017). The opposite is true for Ge, where slow uptake compared to relatively fast silica precipitation drives the overall relationship between observed K_D^{inst} and net precipitation rates. Ultimately, this kinetic regime is temporary (lasting between a few days to a month) and quickly transitions into the equilibrium regime characterized by extensive Ge incorporation at (near) equilibrium conditions where Si concentrations no longer change with time (Fig. 7A,B).

These coupled experimental observations and long-term model predictions largely support an observed rate-dependence in the K_D^{inst} for amorphous silica that is a direct consequence of large differences between Si vs. Ge equilibration timescales. This is a major finding of the study in that: (1) it distinguishes Ge partitioning behavior from other trace elements, notably Sr but also Ba²⁺ and Cd²⁺ (Tesoriero and Pankow, 1996; Prieto et al., 1997), as a function of the timescale of incorporation; (2) it presents for the first time evidence of rate-dependent behavior in Ge partition coefficients; and (3) it provides a "conservative-like" behavior alternative for interpreting rate dependence in the observed K_D^{inst} for other trace elements with similarly slow incorporation kinetics. Thus, variability in the observed K_D^{inst} values we see in nature could reflect a bal-

ance between a "conservative" kinetic K_D , and a "final" equilibrium K_D .

4.6. Toward a Ge/Si and δ^{30} Si multi-tracer approach

Evidence from the experimental data and numerical batch model simulations support the idea of Ge/Si as an equilibrium tracer. Based on this revised viewpoint, we are now poised to interpret the δ^{30} Si vs Ge/Si relationship observed during amorphous silica precipitation (Fig. 2). High precipitation rates at the beginning of the reaction result in a strong, positive correlation between δ^{30} Si and Ge/Si until maximum isotope kinetic enrichment is obtained. Afterwards, as precipitation rates begin to slow down considerably, high surface area δ³⁰Si_{fluid} and (Ge/ Si)_{fluid} display a negative correlation where increasing contributions from equilibrium fractionation return δ^{30} Si_{fluid} to values equivalent to or even lower than the starting composition (referred to as isotopic re-equilibration). Based on the bulk compositions of our experiments, the (Ge/Si)_{fluid} at equilibrium is predicted to range from ~ 0.02 to $0.05 \ \mu mol \ mol^{-1}$. The timescales for $\bar{\delta}^{30} Si$ and Ge/Si fractionation are thus drastically different from one another. δ³⁰Si both kinetically fractionates and experiences subsequent re-equilibration before Ge equilibrium partitioning is even initiated. These δ^{30} Si vs Ge/Si relationships capture a broad range of secondary mineral progression where high δ^{30} Si and Ge/Si ratios reflect early stages of formation and low δ^{30} Si and Ge/Si ratios reflect extensive equilibration.

Extending to timescales common in natural settings, a combination of trace element model fluid Ge/Si ratios under a "surface" mass exchange scenario (Section 4.2) and transient batch model fluid δ^{30} Si (Fernandez et al., 2019) were run out to 20 years for all surface area cases (Fig. 8). This timescale reflects a typical age of older groundwaters in kinetically limited weathering environments (Rademacher et al., 2001, 2005; Manning et al., 2012). The Ge/Si and δ^{30} Si models both predict the extent of equilibrium partitioning to be dependent on the surface area or rate at which the reaction is allowed to proceed. Precipitation results in a quasi-hysteresis loop that reflects an interplay between rapid $\delta^{30}Si$ kinetic fractionation and subsequent re-equilibration towards equilibrium values $(\delta^{30} \text{Si}_{\text{fluid}} = -2.73 \pm 0.07\%$ calculated from the starting fluid ratio, Fernandez et al., 2019, and equilibrium fractionation factor, Stamm et al., 2019) and a slower, continued approach towards predicted (Ge/Si)_{fluid} equilibrium values $(\sim 0.02 \text{ to } 0.05 \text{ } \mu\text{mol mol}^{-1})$ over much longer timescales. Precipitation onto lower surface area amorphous silica seeds significantly slows down growth rates and prolongs both Ge/Si and δ^{30} Si disequilibrium. Thus, lower surface area seeds are able to retain kinetic signatures over much longer timescales.

Another way to visualize these δ^{30} Si vs Ge/Si relationships is through the respective observed Si isotope fractionation factor, (here described via the isotope difference $\Delta_{\text{solid-fluid}} \approx 1000 \times \ln \alpha$) vs. the normalized Ge partition coefficient, KD*, which is here presented in terms of the cumulative precipitate compositions (Fig. 9). In $\Delta_{\text{solid-fluid}}$ vs. K_D* space, a fairly robust negative correlation is observed between the fractionation factor and partition coefficient throughout the course of the experiment. Early stages of amorphous silica growth are associated with an increase in $\Delta_{solid-fluid}$ (due to mixed kinetic and equilibrium fractionation) and a decrease in K_D^{inst} (due to Ge conservative-like behavior). Late stage evolution of high surface area $\Delta_{\text{solid-fluid}}$ and K_{D}^{inst} from model predictions nicely illustrate increasing contributions from Ge/Si equilibrium partitioning (driving the K_D^{inst} up to higher values) as Si stable isotopes approach (near) equilibrium conditions. Based on these findings, fluid Ge/Si and δ^{30} Si may provide significant insight into the fluid residence times within the weathering zone.

Finally, we suggest that δ^{30} Si vs Ge/Si relationships can give constraints on the weathering intensity of a system and the extent of secondary silicate formation where less intense weathering, kinetically limited environments would express high δ^{30} Si and Ge/Si signatures and vice versa for more intensely weathered, transport-limited systems. This application has already been demonstrated for a high weathering intensity, tropical catchment in Costa Rica (Baronas et al., 2020). Therefore, Ge/Si as a (near)equilibrium tracer serves as a complement to δ^{30} Si, which has been demonstrated in

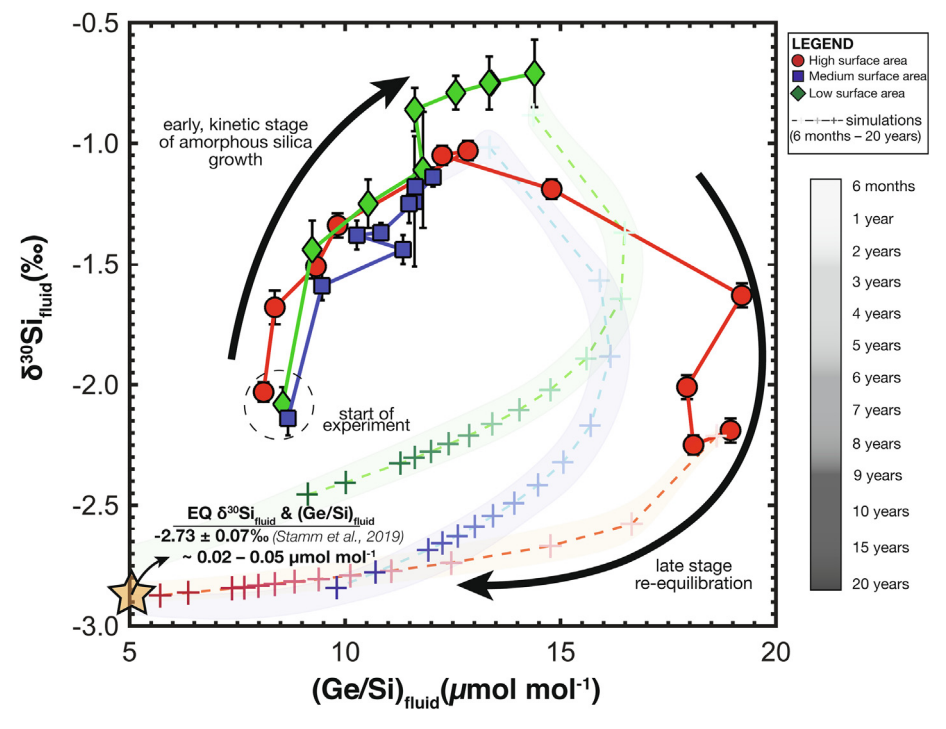


Fig. 8. Measured δ^{30} Si_{fluid} as a function of (Ge/Si)_{fluid} for the surface area batch experiments (depicted as markers) presented alongside trace model predictions for the respective surface area conditions over longer timescales, from 6 months to 20 years. Predicted equilibrium δ^{30} Si_{fluid} and (Ge/Si)_{fluid} are represented by a yellow star, corresponding to values of $-2.73 \pm 0.07\%$, calculated from the measured starting δ^{30} Si_{fluid} (Fernandez et al., 2019) and experimentally constrained equilibrium fractionation factor (Stamm et al., 2019), and $\sim 0.02-0.05 \, \mu mol \, mol^{-1}$, respectively.

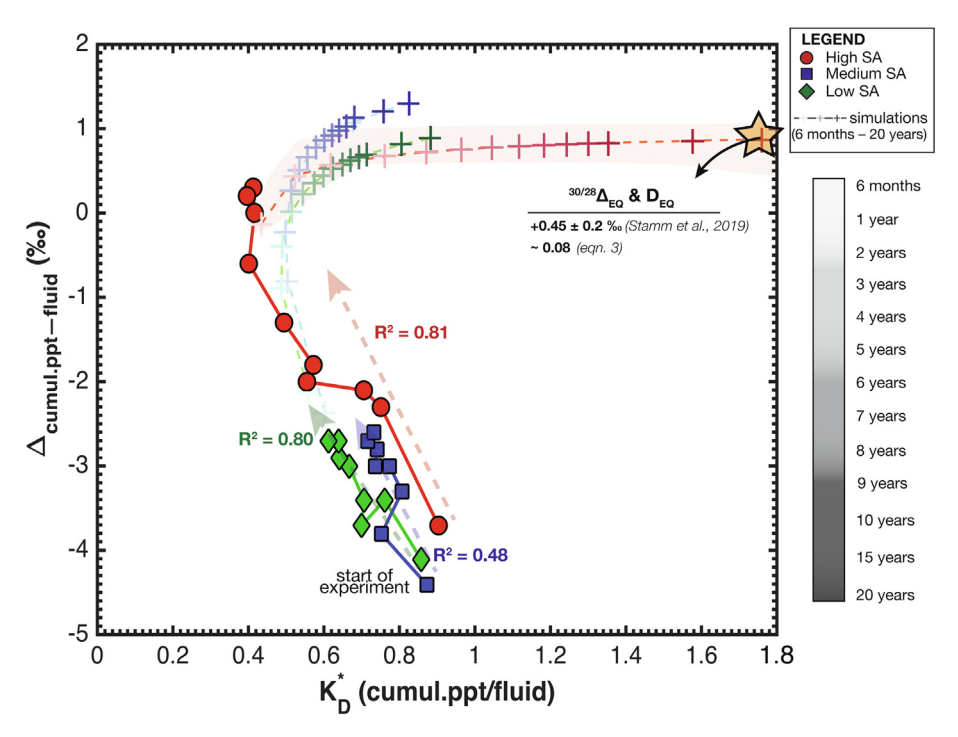


Fig. 9. Calculated observed Si stable isotope fractionation factors, $\Delta_{cumul.ppt-fluid}$, as a function of the normalized instantaneous Ge partition coefficient, K_D^* (i.e. $(Ge/Si)_{fluid} = (Ge/Si)_{am.silica}$), using the composition of the cumulative precipitate as a function of time $((Ge/Si)_{ppt})$. All surface area batch experiments (depicted as markers) are presented alongside trace model fluid $\Delta_{cumul.ppt-fluid}$ and K_D^{inst} predictions from the "surface" simulation (with a time interval > 14 days) from 6 months to 20 years. The equilibrium fractionation factor ($\Delta_{EQ(solid-fluid)}$) and partition coefficient (D_{EQ}) for amorphous silica derives from Stamm et al. (2019) and this study (Eq. (3)), respectively. At 20 years, $\Delta_{cumul.ppt-fluid}$ values suggest that Si stable isotopes are very close to equilibrium in the high surface area case whereas observed K_D^* values at the end of the simulation show that the system is still far from equilibrium for Ge. These results further highlight the distinct equilibration timescales between Ge/Si and δ^{30} Si.

the recent literature to be a tracer of kinetic processes (Geilert et al., 2014; Oelze et al., 2015; Roerdink et al., 2015). Further, the unique behavior of Ge vs. δ^{30} Si with respect to mineralogy serves an added advantage in that the dissolution and precipitation of a given Ge-bearing silicate can be uniquely identified within a given system. This combination of complementary trace element and stable isotope systems represents a path forward in the quantitative analysis of weathering environments, with its potential only now starting to be realized in the literature (Cardinal et al., 2010; Cornelis et al., 2010; Opfergelt et al., 2010; Delvigne et al., 2016; Baronas et al., 2018).

4.7. Ge/Si field signatures from a mixed kinetic-equilibrium partitioning perspective

Finally, we take the opportunity to consider observations from a variety of field-scale systems for which the present study may offer new insight. In transport-limited weathering environments such as large sedimentary basins where groundwater ages can reach millennial timescales (Sturchio et al., 2004), amorphous silica is commonly observed as a cementation or accretion between grains and serves as an important ³⁰Si depleted reservoir (Basile-Doelsch et al., 2005). In this context, timescales may be sufficient to allow slow Ge incorporation to serve as a Ge terrestrial sink. At shorter timescales in kinetically limited

weathering environments, amorphous silica formation is less common and most likely a less important control on observed Ge/Si signatures relative to other secondary phases. However, the range of surface areas encapsulated by this study $(0.07-50.00 \text{ m}^2 \text{ g}^{-1})$ overlap with those observed in both basaltic (2-24 m² g⁻¹; Navarre-Stichler et al., 2015) and granitic $(0.1-1.5 \text{ m}^2 \text{ g}^{-1})$; White et al., 1996) regolith. Thus, our results may be relevant to other secondary silicates and suggest that if slow Ge kinetics are indeed applicable to a variety of secondary clays, then long subsurface fluid transit times would be necessary to create low stream Ge/Si compositions as a result of Ge incorporation into these minerals. If Ge incorporation into secondary clays is slow because of kinetic limitations on either mineral neoformation or Ge incorporation into neoformed phases then adsorption onto Fe and Al (oxy)hydroxides may play a more important role on shorter timescales (Mortlock and Froelich, 1987; Kurtz et al., 2002; Schribner et al., 2006). For instance, batch experiments showed fast Ge uptake rates during for Ge adsorption onto goethite, with $\sim 80\%$ of dissolved Ge removed from solution over the span of 10 minutes and complete Ge incorporation by 100 minutes during coprecipitation with FeOH (Pokrovsky et al., 2006).

Slow Ge kinetics and mixed kinetic and equilibrium Ge partitioning may also hold relevance for the signatures of marine diagenesis. Observations of Ge decoupling from Si at depth in marine sediments rich in biogenic opal spanning 100,000 s of years (Hammond et al., 2000; King et al., 2000; Baronas et al., 2016) have generally been interpreted as reflecting a complex balance between biogenic silica dissolution and (re)precipitation of amorphous silica along with potentially iron-rich clays. From the perspective of our experimental results, decoupling of Ge from Si could reflect the large disparity between fast Si precipitation kinetics and slow Ge recrystallization, yielding observations of Geenriched porewaters with depth into the sediment profile (King et al., 2000).

Finally, results from this study may offer utility in the interpretation of high Ge/Si ratios found in hydrothermal waters (Arnórsson, 1984; Criaud and Fouillac, 1986; Evans and Derry, 2002; Han et al., 2015). Geothermal waters from active geothermal systems have high, but variable (Ge/Si)fluid, which was explained using a Rayleigh model for the precipitation of Ge-depleted quartz along a cooling path(s) (Evans and Derry 2002). Our findings agree with this interpretation where the formation of Ge-depleted amorphous silica would result in elevated (Ge/Si)fluid throughout the experimental duration. However, the successful application of our trace model to the experimental data suggest that a Rayleigh model could be overly simplistic of an approach for amorphous silica where a back reaction is known to occur and would most likely lead to an overestimation of the extent of Ge/Si partitioning. Our combined modeling and experimental study concludes that fluid interaction with the mineral surface dictates the observed (Ge/Si)_{fluid} over the timescales of mineral growth.

5. CONCLUSIONS

This study reports Ge/Si fractionation during amorphous silica precipitation across a range of precipitation rates under highly controlled laboratory settings. Our findings show that Ge incorporation kinetics are very slow (\sim 10 orders of magnitude slower than silica precipitation rates) and, as a result, gives the appearance of conservative behavior over short timescales (\sim 30 days). A major consequence of this observed lag between fast Si kinetics and Ge conservative-like behavior at early stages of mineral growth is the appearance of rate dependence behavior in the observed partition coefficient, KD. Model results imply that Ge/Si fractionation is controlled by equilibrium processes, making it a unique equilibrium tracer. Over long timescales, Ge/Si equilibrium partitioning appears to exhibit dependence on the reaction rate with fluid Ge/Si returning to equilibrium values faster during uptake onto higher surface area seeds relative to lower surface area seeds. A combined δ³⁰Si and Ge/Si multi-tracer approach has the potential to provide important constraints on weathering intensity, fluid residence times and the amount of secondary silicate formation taking place in the weathering zone. Finally, successful application of the trace element batch model to the experimental dataset over a range of surface areas suggests that the framework developed in the CrunchTope software under the assumption that trace elements behave analogously to stable isotopes is valid for δ^{30} Si-Ge/Si system. Our results extend the utility of CrunchTope for modeling

both kinetic and equilibrium trace element partitioning in addition to stable isotope fractionation.

Declaration of Competing Interest

The authors declare that they have no known competing financial interests or personal relationships that could have appeared to influence the work reported in this paper.

ACKNOWLEDGMENTS

This material is based upon work supported by the National Science Foundation Graduate Research Fellowship Program under Grant No. DGE-1144245, NSF grant EAR 1660923, l'Agence Nationale de la Recherche project ANR-17-MPGA-0009, and by the Chateaubriand Fellowship of the Office for Science & Technology of the Embassy of France in the United States. Special acknowledgment is given to Jérôme Gaillardet, Julien Bouchez, and the G2E (Géochimie des Enveloppes Externes) group for their assistance and allowing us access to the facilities at the Institut de Physique du Globe de Paris (IPGP) in Paris, France to perform the experiments and measurements necessary for this study. We extend our thanks to Associate Editor Sophie Opfergelt as well as Jotautas Baronas and two anonymous reviewers for their constructive and detailed reviews that have greatly improved this manuscript.

APPENDIX A. SUPPLEMENTARY MATERIAL

Supplementary data to this article can be found online at https://doi.org/10.1016/j.gca.2021.01.007.

REFERENCES

- Ackermann R. J. and Sorrell C. A. (1974) Thermal expansion and the high-low transformation in quartz. I. High-temperature Xray studies. J. Appl. Crystallogr. 7, 461–467.
- Aguirre A. A., Derry L. A., Mills T. J. and Anderson S. P. (2017) Colloidal transport in the Gordon Gulch catchment of the Boulder Creek CZO and its effect on C-Q relationships for silicon. *Water Resour. Res.* **53**, 2368–2383.
- AlKhatib M. and Eisenhauer A. (2017) Calcium and strontium isotope fractionation in aqueous solutions as a function of temperature and reaction rate: I. Calcite. *Geochim. Cosmochim. Acta* 209, 296–319.
- Ameijeiras-Marino Y., Opfergelt S., Derry L. A., Robinet J., Govers G., Minella J. P. G. and Delmelle P. (2018) Ge/Si ratios point to increased contribution from deeper mineral weathering to streams after forest conversion to cropland. *Appl. Geochem.* **96.** 24–34.
- Anderson G. M. and Crerar D. A. (1993) *Thermodynamics in Geochemistry: The Equilibrium Model*. Oxford University Press, London.
- Arnórsson S. (1984) Germanium in Icelandic geothermal systems. *Geochim. Cosmochim. Acta* **48**, 2489–2502.
- Bard E., Labeyrie L. D., Arnold M., Labracherie M., Pichon J.-L., Duprat J. and Duplessy J.-C. (1989) AMS 14-C ages measured in deep-sea cores from the Southern Ocean: implications for the sedimentation rates during isotope stage 2. *Quat. Res.* 31, 309–317
- Baronas J. J., Hammond D. E., Berelson W. M., McManus J. and Severmann S. (2016) Germanium-silicon fractionation in a river-influenced continental margin: The Northern Gulf of Mexico. Geochim. Cosmochim. Acta 178, 124–142.

- Baronas J. J., Torres M. A., West A. J., Rouxel O., George B., Bouchez J., Gaillardet J. and Hammond D. E. (2018) Ge and Si isotope signatures in rivers: A quantitative multi-proxy approach. *Earth Planet. Sci. Lett.* **503**, 194–215.
- Baronas J. J., West A. J., Burton K. W., Hammond D. E., Opfergelt S., Pogge von Strandmann P. A. E., James R. H. and Rouxel O. J. (2020) Ge and Si isotope behavior during intense tropical weathering and ecosystem cycling. *Global Biogeochem. Cycles* 34, 1–25.
- Basile-Doelsch I., Meunier J. D. and Parron C. (2005) Another continental pool in the terrestrial silicon cycle. *Nature* 433, 399– 402
- Blecker S. W., King S. L., Derry L. A., Chadwick O. A., Ippolito J. A. and Kelly E. F. (2007) The ratio of germanium to silicon in plant phytoliths: quantification of biological discrimination under controlled experimental conditions. *Biogeochemistry* 86, 189–199.
- Böhm F., Eisenhauer A., Tang J., Dietzel M., Krabbenhöft A., Kisakürek B. and Horn C. (2012) Strontium isotope fractionation of planktic foraminifera and inorganic calcite. *Geochim. Cosmochim. Acta* **93**, 300–314.
- Capobianco C. and Navrotsky A. (1982) Calorimetric evidence for ideal mixing of silicon and germanium in glasses and crystals of sodium-feldspar composition. Am. Mineral. 67, 718–724.
- Capobianco C. and Watson E. B. (1981) Olivine/silicate melt partitioning of germanium: an example of a nearly constant partition coefficient. *Geochim. Cosmochim. Acta* 46, 235–240.
- Cardinal D., Gaillardet J., Hughes H. J., Opfergelt S. and André L. (2010) Contrasting silicon isotope signatures in rivers from the Congo Basin and the specific behaviour of organic-rich waters. *Geophys. Res Lett*, 37.
- Cornelis J. T., Delvaux B. and Titeux H. (2010) Contrasting silicon uptakes by coniferous trees: A hydroponic experiment on young seedlings. *Plant Soil* **336**, 99–106.
- Criaud A. and Fouillac C. (1986) Study of CO₂-rich thermomineral waters from the central French massif. 2. Behavior of some trace-metals, arsenic, antimony and germanium. *Geochim. Cosmochim. Acta* **50**, 1573–1582.
- Delvigne C., Opfergelt S., Cardinal D., Hofmann A. and André L. (2016) Desilication in Archean weathering processes traced by silicon isotopes and Ge/Si ratios. *Chem. Geol.* 420, 139–147.
- DePaolo D. J. (2011) Surface kinetic model for isotopic and trace element fractionation during precipitation of calcite from aqueous solutions. *Geochim. Cosmochim. Acta* 75, 1039–1056.
- Derry L. A., Kurtz A. C., Ziegler K. and Chadwick O. A. (2005) Biological control of terrestrial silica cycling and export fluxes to watersheds. *Nature* **433**, 728–731.
- Druhan J. L., Steefel C. I., Williams K. H. and DePaolo D. J. (2013) Calcium isotope fractionation in groundwater: Molecular scale processes influencing field scale behavior. *Geochim. Cosmochim. Acta* 119, 93–116.
- Escoube R., Rouxel O. J., Edwards K., Glazer B. and Donard O. F. X. (2015) Coupled Ge/Si and Ge isotope ratios as geochemical tracers of seafloor hydrothermal systems: Case studies at Loihi Seamount and East Pacific Rise 9°50'N. *Geochim. Cosmochim. Acta* 167, 93–112.
- Evans M. J. and Derry L. A. (2002) Quartz control of high germanium/silicon ratios in geothermal waters. *Geology* 30, 1019–1022.
- Fernandez N. M., Zhang X. and Druhan J. L. (2019) Silicon isotopic re-equilibration during amorphous silica precipitation and implications for isotopic signatures in geochemical proxies. *Geochim. Cosmochim. Acta* 262, 104–127.
- Fleming B. A. (1986) Kinetics of reaction between silicic acid and amorphous silica surfaces in NaCl solutions. *J. Colloid Interface Sci.* **110**, 40–64.

- Frings P. J., Clymans W., Fontorbe G., De La Rocha C. L. and Conley D. J. (2016) The continental Si cycle and its impact on the ocean Si isotope budget. *Chem. Geol.* **425**, 12–36.
- Froelich P. N., Blanc V., Mortlock R. A., Chillrud S. N., Dunstan W., Udomkit A. and Peng T.-H. (1992) River fluxes of dissolved silica to the ocean were higher during glacials: Ge/Si in diatoms, rivers, and oceans. *Paleoceanography* 7, 739–767.
- Froelich P. N., Hambrick G. A., Andreae M. O., Mortlock R. A. and Edmond J. M. (1985) The geochemistry of inorganic germanium in natural waters. J. Geophys. Res. Ocean. 90, 1133–1141
- Froelich P. N., Hambrick G. A., Kaul L. W., Byrd J. T. and Lecointe O. (1984) Geochemical behavior of inorganic germanium in an unperturbed estuary. *Geochim. Cosmochim. Acta* 49, 519–524.
- Gabitov R. I. and Watson E. B. (2006) Partitioning of strontium between calcite and fluid. *Geochem., Geophys. Geosyst.* 7, 1–12.
- Gabitov R. I., Sadekov A. and Leinweber A. (2014) Crystal growth rate effect on Mg/Ca and Sr/Ca partitioning between calcite and fluid: An in situ approach. *Chem. Geol.* **367**, 70–82.
- Geilert S., Vroon P. Z., Roerdink D. L., Van Cappellen P. and van Bergen M. J. (2014) Silicon isotope fractionation during abiotic silica precipitation at low temperatures: Inferences from flow-through experiments. *Geochim. Cosmochim. Acta* 142, 95– 114.
- George R. B., Reynolds B. C., Frank M. and Halliday A. N. (2006) Mechanisms controlling the silicon isotopic compositions of river waters. *Earth Planet. Sci. Lett.* 249, 290–306.
- George R. B., Reynolds B. C., West A. J., Burton K. W. and Halliday A. N. (2007) Silicon isotope variations accompanying basalt weathering in Iceland. *Earth Planet. Sci. Lett.* 261, 476– 490.
- George R. B., Zhu C., Reynolds B. C. and Halliday A. N. (2009) Stable silicon isotopes of groundwater, feldspars, and clay coatings in the Navajo Sandstone aquifer, Black Mesa, Arizona, USA. Geochim. Cosmochim. Acta 73, 2229–2241.
- Gleeson T., Befus K. M., Jasechko S., Luijendijk E. and Bayani C. M. (2015) The global volume and distribution of modern groundwater. *Nature* 9, 161–167.
- Goldschmidt V. M. (1926) Concerning the crystallo-chemical and geochemical behavior of Germanium. *Naturwissenschaften* 14, 295–297.
- Goldschimdt V. M. (1958) Geochemistry. Oxford University Press, London.
- Gresens R. L. (1981) The aqueous solubility product of solid solutions: 1. Stoichiometric saturation: partial and total solubility product. *Chem. Geol.* 32, 59–72.
- Gunnarsson I. and Anórsson S. (2000) Amorphous silica solubility and the thermodynamic properties of H4SiO°4 in the range of 0° to 350°C at Psat. *Geochim. Cosmochim. Acta* **64**, 2295–2307.
- Hammond D. E., McManus J., Berelson W. M., Meredith C., Klinkhammer G. P. and Coale K. H. (2000) Diagenetic fractionation of Ge and Si in reducing sediments: The missing Ge sink and a possible mechanism to cause glacial/interglacial variations in oceanic Ge/Si. Geochim. Cosmochim. Acta 64, 2453–2465.
- Han Y., Huh Y. and Derry L. (2015) Ge/Si ratios indicating hydrothermal and sulfide weathering input to rivers of the Eastern Tibetan Plateau and Mt, Baekdu. *Chem. Geol.* 410, 40– 52
- Heumann K. G. (1988) Isotope Dilution Mass Spectrometry. In Inorganic Mass Spectrometry (eds. F. Adams, R. Gijbels and R. van Grieken). John Wiley & Sons, New York, NY.
- Huang Y. and Fairchild I. J. (2001) Partitioning of Sr2+ and Mg2
 + into calcite under karst-analogue experimental conditions.
 Geochim. Cosmochim. Acta 65, 47–62.

- Hughes H. J., Sondag F., Santos R. V., André L. and Cardinal D. (2013) The riverine silicon isotope composition of the Amazon Basin. Geochim. Cosmochim. Acta 121, 637–651.
- Iler R. K. (1979) The Chemistry of Silica: Solubility, Polymerization, Colloid and Surface Chemistry, and Biochemistry. John Wiley & Sons.
- King S. L., Froelich P. N. and Jahnke R. A. (2000) Early diagenesis of germanium in sediments of the Antarctic South Atlantic: In search of the missing Ge sink. *Geochim. Cosmochim. Acta* 64, 1375–1390
- Kurtz A. C., Derry L. A. and Chadwick O. A. (2002) Germaniumsilicon fractionation in the weathering environment. *Geochim. Cosmochim. Acta* 66, 1525–1537.
- Kurtz A. C., Lugolobi F. and Salvucci G. (2011) Germaniumsilicon as a flow path tracer: Application to the Rio Icacos watershed. Water Resour. Res. 47, 1–16.
- Lichtner P. C. (1988) The quasi-stationary state approximation to coupled mass transport and fluid-rock interaction in a porous medium. *Geochim. Cosmochim. Acta* **52**, 143–165.
- Lorens R. B. (1981) Sr, Cd, Mn and Co distribution coefficients in calcite as a function of calcite precipitation rate. *Geochim. Cosmochim. Acta* 45, 553–561.
- Lugolobi F., Kurtz A. C. and Derry L. A. (2010) Germaniumsilicon fractionation in a tropical, granitic weathering environment. *Geochim. Cosmochim. Acta* 74, 1294–1308.
- Manning A. H., Clark J. F., Diaz S. H., Rademacher L. K., Earman S. and Plummer L. N. (2012) Evolution of groundwater age in a mountain watershed over a period of thirteen years. *J. Hydrol.* **460–461**, 13–28.
- Martin F., Ildefonse P., Hazemann J. L., Petit S., Grauby O. and Decarreau A. (1996) Random distribution of Ge and Si in synthetic talc: An EXAFS and FTIR study. *Eur. J. Mineral.* **8**, 289–299.
- Meek K., Derry L., Sparks J. and Cathles L. (2016) 87/86Sr, Ca/Sr, and Ge/Si ratios as tracers of solute sources and biogeochemical cycling at a temperate forested shale catchment, central Pennsylvania, USA. Chem. Geol. 445, 84–102.
- Mortlock R. A. and Froelich P. N. (1987) Continental weathering of germanium: Ge/Si in the global river discharge. *Geochim. Cosmochim. Acta* 51, 2075–2082.
- Mortlock R. A. and Froelich P. N. (1996) Determination of germanium by isotope dilution hydride generation inductively coupled plasma mass spectrometry. *Anal. Chim. Acta* **332**, 277–284.
- Mortlock R. A., Charles C. D., Froelich P. N., Zibello M. A., Saltzman J., Hays J. D. and Burckle L. H. (1991) Evidence for lower productivity in the Antarctic Ocean during the last glaciation. *Nature* 351, 220–222.
- Murnane R. J. and Stallard R. F. (1990) Germanium and silicon in rivers of the Orinoco drainage basin. *Nature* **344**, 749.
- Navarre-Stichler A., Brantley S. L. and Rother G. (2015) How porosity increases during incipient weathering of crystalline silicate rocks. Reviews Mineral. Geochem. 80, 331–354.
- Nehrke G., Reichart G. J., Van Cappellen P., Meile C. and Bijma J. (2007) Dependence of calcite growth rate and Sr partitioning on solution stoichiometry: Non-Kossel crystal growth. *Geochim. Cosmochim. Acta* 71, 2240–2249.
- Noiriel C., Luquot L., Madé B., Raimbault L., Gouze P., and van der Lee J. (2009) Changes in reactive surface area during limestone dissolution: An experimental and modeling study. Chem. Geol. 265, 160–170.https://www.nature.com/articles/ 344749a0
- Oelze M., von Blanckenburg F., Bouchez J., Hoellen D. and Dietzel M. (2015) The effect of Al on Si isotope fractionation investigated by silica precipitation experiments. *Chem. Geol.* **397**, 94–105.

- Opfergelt S., Cardinal D., André L., Delvigne C., Bremond L. and Delvaux B. (2010) Variations of δ³⁰Si and Ge/Si with weathering and biogenic input in tropical basaltic ash soils under monoculture. *Geochim. Cosmochim. Acta* **74**, 225–240.
- Opfergelt S. and Delmelle P. (2012) Silicon isotopes and continental weathering processes: Assessing controls on Si transfer to the ocean. *Comptes Rendus Geosci.* **344**, 723–738.
- Perez-Fodich A. and Derry L. A. (2020) A model for germaniumsilicon equilibrium fractionation in kaolinite. *Geochim. Cos*mochim. Acta 288, 199–213.
- Pogge von Strandmann P. A. E., Opfergelt S., Lai Y.-J., Sigfússon B., Gislason S. R. and Burton K. W. (2012) Lithium, magnesium and silicon isotope behaviour accompanying weathering in a basaltic soil and pore water profile in Iceland. *Earth Planet. Sci. Lett.* 339–340, 11–23.
- Pokrovski G. S. and Schott J. (1998) Experimental study of the complexation of silicon and germanium with aqueous organic species: implications for germanium and silicon transport and Ge/Si ratio in natural waters. *Geochim. Cosmochim. Acta* 62, 3413–3428.
- Pokrovski G. S., Roux J., Hazemann J.-L. and Testemale D. (2005) An X-ray absorption spectroscopy study of argutite solubility and aqueous Ge(IV) speciation in hydrothermal fluids to 500 °C and 400 bar. *Chem. Geo.* **217**, 127–145.
- Pokrovsky O. S., Pokrovski G. S., Schott J. and Galy A. (2006) Experimental study of germanium adsorption on goethite and germanium coprecipitation with iron hydroxide: X-ray absorption fine structure and macroscopic characterization. *Geochim. Cosmochim. Acta* 70, 3325–3341.
- Prieto M., Fernández-González A., Putnis A. and Fernández-Díaz L. (1997) Nucleation, growth, and zoning phenomena in crystallzing (Ba, Sr)CO3, Ba(SO4, CrO4), (Ba, Sr)SO4, and (Cd, Ca)CO3 solid solutions from aqueous solutions. *Geochim. Cosmochim. Acta* 61, 3383–3397.
- Qi H. W., Hu R. Z., Jiang K., Zhou T., Liu Y. F. and Xiong Y. W. (2019) Germanium isotopes and Ge/Si fractionation under extreme tropical weathering of basalts from the Hainan Island, South China. Geochim. Cosmochim. Acta 253, 249–266.
- Rademacher L. K., Clark J. F., Clow D. W. and Hudson G. B. (2005) Old groundwater influence on stream hydrochemistry and catchment response times in a small Sierra Nevada catchment: Sagehen Creek, California. Water. Resour. Res. 41, 1–10.
- Rademacher L. K., Clark J. F., Hudson G. B., Erman D. C. and Erman N. A. (2001) Chemical evolution of shallow groundwater as recorded by springs, Sagehen basin, Nevada County, California. *Chem. Geol.* 179, 37–51.
- Rimstidt J. D. and Barnes H. L. (1980) The kinetics of silica-water reactions. Geochim. Cosmochim. Acta 44, 1683–1699.
- Riotte J., Meunier J.-D., Zambardi T., Audry S., Barboni D., Anupama K., Prasad S., Chmeleff J., Poitrasson F., Sekhar M. and Braun J.-J. (2018) Processes controlling silicon isotopic fractionation in a forested tropical watershed: Mule Hole Critical Zone Observatory (Southern India). Geochim. Cosmochim. Acta 228, 301–319.
- Roerdink D. L., van den Boorn S. H. J. M., Geilert S., Vroon P. Z. and van Bergen M. J. (2015) Experimental constraints on kinetic and equilibrium silicon isotope fractionation during the formation of non-biogenic chert deposits. *Chem. Geol.* 402, 40–51.
- Scribner A. M., Kurtz A. C. and Chadwick O. A. (2006) Germanium sequestration by soil: Targeting the roles of secondary clays and Fe-oxyhydroxides. *Earth Planet. Sci. Lett.* 243, 760–770.
- Shtenberg M. V., Bychinskii V. A., Koroleva O. N., Korobatova N. M., Tupitsyn A. A., Fomichev S. V. and Krenev V. A. (2017) Calculation of the formation enthalpies, standard

- entropies, and standard heat capacities of alkali and alkalineearth germanates. *Russ. J. Inorg. Chem.* **62**, 1464–1468.
- Stamm F. M., Zambardi T., Chmeleff J., Schott J., von Blacnkenburg F. and Oelkers E. H. (2019) The experimental determination of equilibrium Si isotope fractionation factors among H₄SiO₄, H₃SiO₄ and amorphous silica (SiO₂ 0.32 H2O) at 25 and 75°C using the three-isotope method. *Geochim. Cosmochim. Acta* 255, 49–68.
- Steefel C. I., Druhan J. L. and Maher K. (2014) Modeling coupled chemical and isotopic equilibration rates. *Procedia Earth Planet.* 10, 208–217.
- Steefel C. I., Yabusaki S. B. and Mayer K. U. (2015) Reactive transport benchmarks for subsurface environmental simulation. *Comput. Geosci.* 19, 439–443.
- Sturchio N.C., Du X., Purtschert R., Lehmann B.E., Sultan M., Patterson L.J. Müller P., Bigler T., Bailey K., O'Connor T.P., Young L., Lorenzo R., Becker R., El Alfy Z., Kaliouby B.El. Dawood Y., and Abdallah A.M.A. One million year old groundwater in the Sahara revealed by krypton-81 and chlorine-36. Geophys. Res. Lett. 31, 1-4.
- Tang J., Köhler S. J. and Dietzel M. (2008) Sr2+/Ca2+ and 44Ca/ 40Ca fractionation during inorganic calcite formation: I. Sr Incorporation. *Geochim. Cosmochim. Acta* 72, 3718–3732.
- Tesoriero A. J. and Pankow J. F. (1996) Solid solution partitioning of Sr²⁺, Ba²⁺, and Cd²⁺ to calcite. *Geochim. Cosmochim. Acta* **60**, 1053–1063.
- Tobler D. J., Shaw S. and Benning L. G. (2009) Quantification of initial steps of nucleation and growth of silica nanoparticles: An in-situ SAXS and DLS study. *Geochim. Cosmochim. Acta* 73, 5377–5393.
- Tréguer P., Nelson D. M., van Bennekom A. J., DeMaster D. J., Leynaert A. and Quéguiner B. (1995) The balance of silica in the world oceans: a re-estimate. *Science* **268**, 375–379.
- Wada S. and Wada K. (1982) Effects of substitution of germanium for silicon in imogolite. *Clays Clay Miner.* **30**, 123–128.

- Wasylenki L. E., Dove P. M., Wilson D. S. and De Yoreo J. J. (2005) Nanoscale effects of strontium on calcite growth: An insitu AFM study in the absence of vital effects. *Geochim. Comochim. Acta* 69, 3017–3027.
- White A. F., Blum A. E., Schulz M. S., Bullen T. D., Harden J. W. and Peterson M. L. (1996) Chemical weathering rates of a soil chronosequence on granitic alluvium: I. Quantification of mineralogical and surface area changes and calculation of primary silicate reaction rates. *Geochim. Cosmochim. Acta* 60, 2533–2550.
- Wright A. F. and Lehmann M. S. (1981) The structure of quartz at 25 and 590°C determined by neutron diffraction. *J. Solid State Chem.* **36**, 371–380.
- Yang L. and Steefel C. (2008) Kaolinite dissolution and precipitation kinetics at 22°C and pH 4. *Geochim. Cosmochim. Acta* 72, 99–116.
- Zheng X.-Y., Beard B. L. and Johnson C. M. (2019) Constraining silicon isotope exchange kinetics and fractionation between aqueous and amorphous Si at room temperature. *Geochim. Cosmochim. Acta* 253, 267–289.
- Zhu C., Rimstidt J. D., Zhang Y. L., Kang J. T., Schott J. and Yuan H. L. (2020) Decoupling feldspar dissolution and precipitation rates at near-equilibrium with Si isotope tracers: Implications for modeling silicate weathering. *Geochim. Cos-mochim. Acta* 271, 132–153.
- Ziegler K., Chadwick O. A., Brwewinski M. A. and Kelly E. F. (2005a) Natural variations of δ^{30} Si ratios during progressive basalt weathering, Hawaiian Islands. *Geochim. Cosmochim. Acta* **69**, 4597–5461.
- Ziegler K., Chadwick O. A., White A. F. and Brzezinski M. A. (2005b) δ^{30} Si systematics in a granitic saprolite, Puerto Rico. *Geology* **33**, 817–820.

Associate editor: Sophie Opfergelt